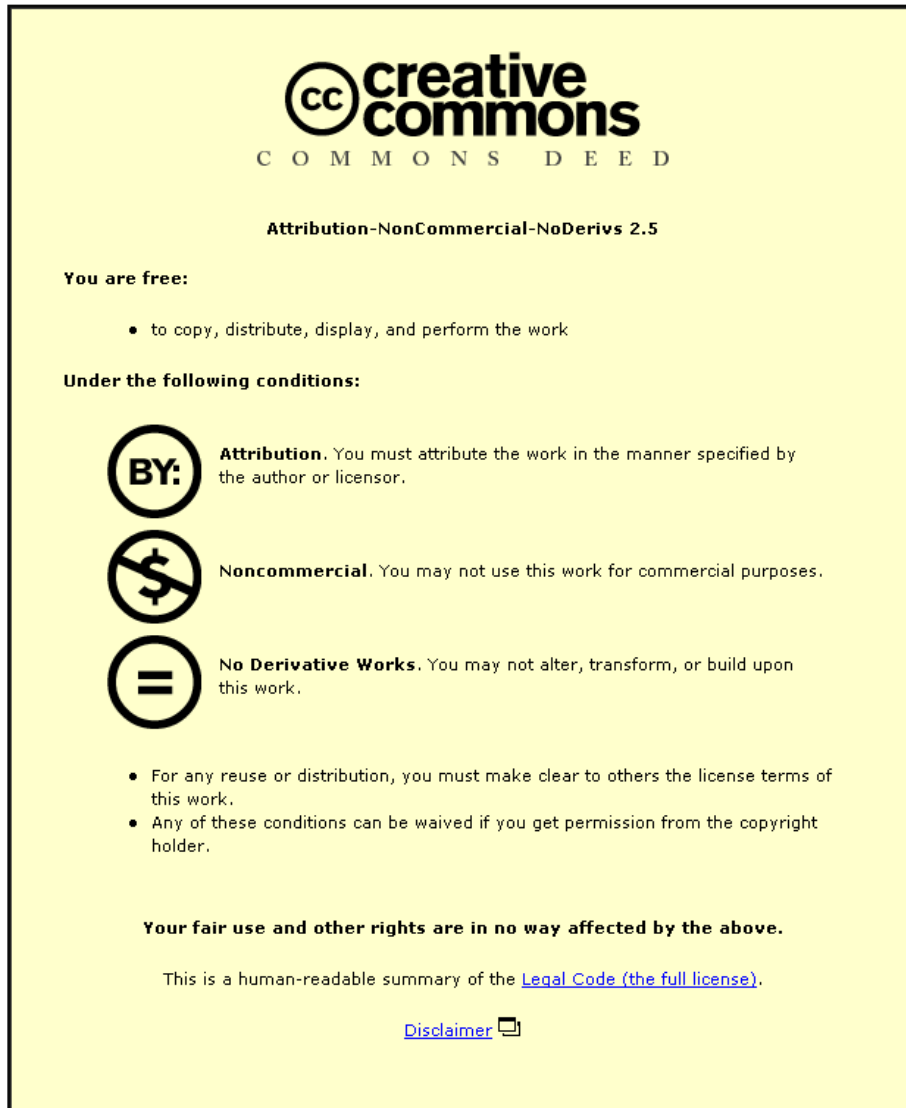


This item was submitted to Loughborough's Institutional Repository (<https://dspace.lboro.ac.uk/>) by the author and is made available under the following Creative Commons Licence conditions.



CC creative commons
COMMONS DEED

Attribution-NonCommercial-NoDerivs 2.5

You are free:

- to copy, distribute, display, and perform the work

Under the following conditions:

BY: **Attribution.** You must attribute the work in the manner specified by the author or licensor.

Noncommercial. You may not use this work for commercial purposes.

No Derivative Works. You may not alter, transform, or build upon this work.

- For any reuse or distribution, you must make clear to others the license terms of this work.
- Any of these conditions can be waived if you get permission from the copyright holder.

Your fair use and other rights are in no way affected by the above.

This is a human-readable summary of the [Legal Code \(the full license\)](#).

[Disclaimer](#) 

For the full text of this licence, please go to:
<http://creativecommons.org/licenses/by-nc-nd/2.5/>

Prediction of a non-isothermal three-dimensional mixing layer created by a scarfed lobed mixer

H Salman[†], J J McGuirk, and G J Page*

Department of Aeronautical and Automotive Engineering, Loughborough University, Loughborough, Leicestershire, UK

The manuscript was received on 28 November 2005 and was accepted after revision for publication on 6 April 2006.

DOI: 10.1243/09544100JAERO66

Abstract: The work presented here considers the complex mixing processes associated with a three-dimensional non-isothermal convoluted mixing layer such as produced by scarfed lobed mixers as used in aero-engine gas turbine exhaust ducts. Numerical simulations of the compressible Navier–Stokes equations in Reynolds-averaged form with a $k-\varepsilon$ turbulence model are conducted. The discretization of the high-Reynolds-number form of the $k-\varepsilon$ model for the unstructured mesh numerical solver used is described. The discretization was verified against two elemental flows that represent subcomponents of lobed mixer problems: a planar shear layer and a developing boundary layer. A grid dependency study is also presented for different grid types: purely quadrilateral, a purely triangular, and a mixed grid, to assess the influence of different mesh types on predictions. Results for a two-dimensional planar shear layer flow indicated that quadrilateral grids yielded best results for a given grid resolution. This result was confirmed in the numerical simulations of three-dimensional convoluted shear layers created by a generic lobed mixer geometry in which hexahedral grids yielded the most accurate results relative to a purely tetrahedral grid and a mixed grid. The model was finally used to simulate the flow field in an engine-representative scarfed mixer configuration under non-isothermal flow conditions representative of current engine practice. Results showed that the scarfed mixer introduced strong flow asymmetries in the azimuthal direction. This caused adjacent vortical structures produced by the alternating short and long gullies of the lobes to interact with one another and this behaviour dominated the flow evolution. Detailed comparisons between predicted and measured temperature fields were also carried out and generally showed encouraging agreement and capture of correct trends. The evolution of the predicted thermal mixing layer slightly lagged the measured data as was also the case for the velocity fields, indicating that improvements in the prediction of the thermal mixing layer may be strongly dependent on correct prediction of the momentum transport process as well as improved modelling of the turbulent heat fluxes.

Keywords: gas turbine, forced mixer, lobed mixer, computational fluid dynamics

1 INTRODUCTION

Advances in computational methods have produced a growing interest in simulating lobed mixer flows,

which are an important component of achieving low specific fuel consumption in several modern gas turbine turbofan engines [1–4]. Lobed mixers contribute to improved engine efficiency and also to reduced jet noise because they lead to a more uniform radial profile emerging from the engine exhaust. This is achieved via extra convective stirring of fan and core streams by creation of streamwise vorticity downstream of the lobed mixer. Clearly, this has to be accomplished at minimum extra weight and pressure drag penalties, and optimum lobed mixer design represents a considerable

*Corresponding author: Department of Aeronautical and Automotive Engineering, Loughborough University, Ashby Road, Loughborough, Leicestershire, LE11 3TU, UK. email: g.j.page@lboro.ac.uk

[†]Now at: Mathematics Department, Phillips Hall, UNC-Chapel Hill, Chapel Hill, NC 27599, USA.

engineering challenge. To assess the applicability of the computational models used in simulating these flows, detailed validation studies are needed to compare predictions with experiments. In particular, the choice of the turbulence model employed can have a significant impact on the accurate prediction of these flows. Of the various studies that have been conducted to date, the most detailed validation studies include the works of Koutmos and McGuirk [5] and Salman *et al.* [6, 7]. The simulations of Koutmos and McGuirk were the first to model the flow around a complete lobed mixer geometry using a Reynolds-averaged formulation with a $k-\varepsilon$ turbulence model. Although validation of the method against detailed experimental measurements was considered, a fully conclusive outcome on the performance of the model could not be completed. Salman *et al.* [6, 7] performed detailed validation against the experimental measurements of Yu and Yip [8] and McCormick and Bennett [9]. By comparing both mean and turbulence quantities, it was shown that good engineering predictions can be made of global parameters such as the axial development of shear layer momentum thickness and streamwise circulation. For local mean flow velocity and turbulent Reynolds stresses, predictions indicated a lag in the development of the convoluted shear layer with respect to measurements.

The validation studies conducted on all of these lobed mixer flows were for idealized (usually coplanar) configurations and for isothermal flow conditions only. In practice, however, lobed mixers are of more complex (scarfed and scalloped) geometry and primarily used to mix the cold bypass stream with the hot core flow of a turbofan engine. This gives rise to mixing and transfer of both momentum and thermal energy between the two streams. Although validation studies under isothermal flow conditions provided significant insight into the ability of the model to capture the momentum exchange between the two streams, a proper assessment of the ability to predict the temperature field is lacking. One important issue to address, therefore, is to what extent can predictions with a $k-\varepsilon$ turbulence model reproduce the three-dimensional convoluted thermal mixing layer associated with lobed mixer flows. To address this point, a simulation of the fully compressible Navier–Stokes equations in the Favre-averaged form is required to predict the temperature distribution within the mixing duct downstream of the mixer. Corresponding temperature measurements will also be needed to validate the computed flow. Such an experimental study of a model scale, but engine-representative, lobed mixer with a detailed survey of the temperature field was recently carried out by Mead [10]. The temperature field was measured at two planes transverse to the mean

flow direction downstream of the mixer. The three-dimensional scarfed lobed mixer geometry and operating conditions used in these measurements were typical of mixers found on modern gas turbine engines. A scarfed mixer differs from a coplanar lobed mixer in that the length of adjacent lobe gullies alternately varies between short and long. Such lobed mixer configurations have been found to produce increased mixing rates relative to planar mixer configurations. This has resulted in the widespread deployment of scarfed mixers (and related designs such as scalloped mixers) in real engines, although the precise mechanism that allows scarfed geometries to achieve improved performance is poorly understood.

Scarfig introduces significant computational challenges in simulating the mixer flow field. In particular, generating appropriate computational grids that allow stable and accurate simulations to be performed is non-trivial, as evidenced by other investigators [1, 2, 11], who employed structured or block-structured grids in their simulations of non-scarfed lobe geometries. An alternative approach would be to employ unstructured tetrahedral grids, as was carried out in the parametric studies of O'Sullivan *et al.* [3]. This latter investigation did not, however, address the accuracy and validity of the predicted vorticity-dominated mixing regions. The suitability of unstructured tetrahedral meshes for these complex flows remains, therefore, unclear and to clarify this was the first objective of the present study.

To establish whether unstructured numerical schemes best resolve the complications that arise in simulating realistic lobed mixer flows, the second objective of the work was to assess the influence of different mesh types on the predictability of developing convoluted shear layers. An initial study of this issue was reported in reference [6]. The aim here was to identify and isolate any important numerical artefacts before focusing on the validation of the physical causes of convoluted thermal shear layer predictions. To achieve this goal, an unstructured/mixed grid algorithm is employed, which allows solution of the compressible form of the Navier–Stokes equations on different grid types. This motivated the use of three different grid types to identify the optimum grid for simulating the lobed mixer flow: purely hexahedral, purely tetrahedral, and a mixed grid. Given the questions to be addressed, three key objectives were, therefore, identified for the present work. The first objective was the addition and verification of the $k-\varepsilon$ turbulence model into the unstructured mesh numerical algorithm employed. The second objective was to gain an understanding of how the numerical prediction of complex free shear flows depends on the type of grid being employed in their simulation. Finally,

the third objective was to gain a fundamental understanding of the flow field changes brought about by the introduction of scarfing and the associated effects on the prediction of the thermal mixing layer.

To present these contributions, the remainder of the article is divided into five sections. The mathematical model is presented in section 2. Section 3 is the description of the discretization method chosen for the k - ε turbulence model equations. Section 4 describes the two mixer configurations simulated in the present work and their corresponding flow conditions. Section 5 discusses various grid discretization issues and outlines the approach adopted in the present work to study them. Results are then presented for three separate flows, a planar shear layer, a boundary layer, and finally, a scarfed lobed mixer flow. Finally, conclusions and recommendations for future work are given.

2 MATHEMATICAL MODEL

The mathematical model is based on the compressible Navier–Stokes equations in the Favre-averaged form. These can be written using Cartesian tensor notation as

$$\frac{\partial \rho}{\partial t} + \frac{\partial \rho u_j}{\partial x_j} = 0 \quad (1)$$

$$\frac{\partial \rho u_i}{\partial t} + \frac{\partial}{\partial x_j} (\rho u_i u_j) = -\frac{\partial p}{\partial x_i} + \frac{\partial \tau_{ij}}{\partial x_j} + \frac{\partial}{\partial x_j} (-\overline{\rho u'_i u'_j}) \quad (2)$$

$$\begin{aligned} \frac{\partial \rho E}{\partial t} + \frac{\partial}{\partial x_j} (\rho H u_j) = & -\frac{\partial q_j}{\partial x_j} + \frac{\partial \tau_{ij} u_i}{\partial x_j} + \frac{\partial}{\partial x_j} (-\overline{\rho u'_i u'_j u_i}) \\ & + \frac{\partial}{\partial x_j} (-\overline{\rho H' u'_j}) \end{aligned} \quad (3)$$

where

$$\tau_{ij} = \mu \left(\frac{\partial u_i}{\partial x_j} + \frac{\partial u_j}{\partial x_i} \right) - \frac{2}{3} \mu \frac{\partial u_k}{\partial x_k} \delta_{ij} \quad (4)$$

and

$$q_i = -\kappa \frac{\partial T}{\partial x_i}, \quad p = \rho RT = (\gamma - 1) \rho \left(E - \frac{1}{2} u_i u_i \right) \quad (5)$$

$$p = \rho RT = (\gamma - 1) \rho \left(E - \frac{1}{2} u_i u_i \right) \quad (6)$$

γ is the ratio of specific heat, which is taken as equal to 1.4. The viscosity $\mu(T)$ in the viscous stress expression is assumed to vary with temperature, according to Sutherland's law. ρ and p are Reynolds unweighted time-averaged properties, whereas u_i , E , H , and T are density-weighted Favre-averaged properties. The Reynolds stresses ($\overline{\rho u'_i u'_j}$) have been

modelled using the standard high-Reynolds-number k - ε turbulence model equations of Launder and Spalding [12]. This can be written as

$$\frac{\partial \rho k}{\partial t} + \frac{\partial \rho k u_j}{\partial x_j} = \frac{\partial}{\partial x_j} \left[\left(\mu + \frac{\mu_t}{\sigma_k} \right) \frac{\partial k}{\partial x_j} \right] + P_k - \rho \varepsilon \quad (7)$$

$$\frac{\partial \rho \varepsilon}{\partial t} + \frac{\partial \rho \varepsilon u_j}{\partial x_j} = \frac{\partial}{\partial x_j} \left[\left(\mu + \frac{\mu_t}{\sigma_\varepsilon} \right) \frac{\partial \varepsilon}{\partial x_j} \right] + \frac{\varepsilon}{k} (C_{\varepsilon 1} P_k - C_{\varepsilon 2} \rho \varepsilon) \quad (8)$$

$$\mu_t = C_\mu \frac{\rho k^2}{\varepsilon} \quad (9)$$

$$\begin{aligned} C_\mu = 0.09, \quad \sigma_k = 1.0, \quad \sigma_\varepsilon = 1.3, \\ C_{\varepsilon 1} = 1.44, \quad C_{\varepsilon 2} = 1.92 \end{aligned} \quad (10)$$

Following Liu and Zheng [13], the production term P_k appearing in the source terms of the turbulence equations is written in the following form

$$\begin{aligned} P_k = \mu_t [2(\tilde{s}_{11}^2 + \tilde{s}_{22}^2 + \tilde{s}_{33}^2) \\ + 4(\tilde{s}_{12}^2 + \tilde{s}_{13}^2 + \tilde{s}_{23}^2)] - \left(\frac{2}{3} \frac{\partial u_i}{\partial x_i} \rho k \right) \\ \tilde{s}_{ij} = \left[\frac{1}{2} \left(\frac{\partial u_i}{\partial x_j} + \frac{\partial u_j}{\partial x_i} \right) - \frac{1}{3} \frac{\partial u_k}{\partial x_k} \delta_{ij} \right] \end{aligned} \quad (11)$$

This particular form is useful in that it shows that the production term consists of a part which is always positive and a term whose sign is dependent on local conditions. This distinction between positive and (possibly) negative parts of P_k becomes important when addressing the time integration of the turbulence equations, as discussed in the next section.

The effective (i.e. sum of viscous and turbulent) stresses are given by

$$\begin{aligned} \tau_{ij} - \overline{\rho u'_i u'_j} = (\mu + \mu_t) \left(\frac{\partial u_i}{\partial x_j} + \frac{\partial u_j}{\partial x_i} \right) - \frac{2}{3} (\mu + \mu_t) \\ \times \frac{\partial u_k}{\partial x_k} \delta_{ij} - \frac{2}{3} \rho k \delta_{ij} \end{aligned} \quad (12)$$

The effective (i.e. sum of molecular and turbulent) heat fluxes are given by

$$q_i + \overline{\rho h' u'_i} = -(\kappa + \kappa_t) \frac{\partial T}{\partial x_i} \quad (13)$$

$$\kappa = \frac{\mu C_p}{Pr}, \quad \kappa_t = \frac{\mu_t C_p}{Pr_t} \quad (14)$$

In this work, the molecular (Pr) and turbulent (Pr_t) Prandtl numbers were set to 0.72 and 0.9, respectively.

3 NUMERICAL DISCRETIZATION

The system of equations (1) to (14) comprises a closed set of equations. Solutions are obtained using an unstructured finite volume discretization employing median dual control volumes with a formulation given in terms of an edge-based data structure [14]. This yields a generic formulation allowing different element types to be handled more easily. The discretization of the inviscid fluxes in all transport equations corresponds to central differencing plus a fourth-order smoothing term. The fourth-order smoothing is reformulated in terms of a modified pseudo-Laplacian [15] to improve the accuracy of the scheme in regions where the mesh is not smooth. Monotonic resolution of flow features associated with sharp spatial gradients is obtained by constructing the smoothing operator to include a blend of second- and fourth-order differences. The blending is introduced in the form of a non-linear limiter.

The $k-\varepsilon$ turbulence equations are coupled to the mean flow equations through the eddy viscosity μ_t . This weak coupling between the two systems of equations motivates a decoupled solution procedure, in which the two systems are solved separately rather than as one complete system. This approach has also been used by other workers including references [16–19] and has the advantage of providing code modularity for a range of turbulence models. Denoting the conservative turbulent state vector by $\mathbf{Q} = (\rho k, \rho \varepsilon)^T$ and the convective fluxes of \mathbf{Q} by $\mathbf{F} = (\rho k \mathbf{u} \cdot \mathbf{n}, \rho \varepsilon \mathbf{u} \cdot \mathbf{n})$, the discrete convective fluxes can be written as

$$F_{ij} = \frac{1}{2} [F_{ij}(\mathbf{Q}_i, \mathbf{n}_{ij}) + F_{ij}(\mathbf{Q}_j, \mathbf{n}_{ij})] - \frac{1}{2} |A_{ij}| \left\{ -\frac{1}{3} (1 - \Psi) [\hat{L}_i^{lp}(\mathbf{Q}) - \hat{L}_j^{lp}(\mathbf{Q})] + \Psi(\mathbf{Q}_i - \mathbf{Q}_j) \right\} \tag{15}$$

where $|A|$ is the Jacobian matrix given by

$$|A| = \begin{pmatrix} |\mathbf{u} \cdot \mathbf{n}| & 0 \\ 0 & |\mathbf{u} \cdot \mathbf{n}| \end{pmatrix} \tag{16}$$

and \mathbf{n} is the unit outward normal for the face lying between nodes i and j . For consistency, the linearity preserving pseudo-Laplacian $\hat{L}^{lp}(\mathbf{Q})$ used in the momentum equations is also used in the convective fluxes of turbulence properties

$$\hat{L}_j^{lp}(\mathbf{Q}) = \hat{L}_j(\mathbf{Q}) - \nabla \mathbf{Q} \cdot L_j(\mathbf{x}) \tag{17}$$

$$\hat{L}_j(\mathbf{Q}) = \left(\sum_{i \in E_j} \frac{1}{|\mathbf{x}_j - \mathbf{x}_i|} \right)^{-1} \sum_{i \in E_j} \frac{(\mathbf{Q}_j - \mathbf{Q}_i)}{|\mathbf{x}_j - \mathbf{x}_i|} \tag{18}$$

where $L_j(\mathbf{x}) = (L_j x, L_j y, L_j z)^T$ and E_j is the set of control volumes sharing a common face with control volume j . The linearity preserving pseudo-Laplacian corresponds to a fourth-order dissipation. To resolve high gradients of the turbulence field monotonically, a blending with a second-order dissipation term is employed through a limiter Ψ . The limiter used in this work is given by

$$\Psi = \min \left[\varepsilon^{(2)} \left(\frac{|L_i^{lp}(\phi)|}{|L_i^{lp}(\phi)| + 2\phi_i} + \frac{|L_j^{lp}(\phi)|}{|L_j^{lp}(\phi)| + 2\phi_j} \right), 1 \right] \tag{19}$$

where ϕ is used to represent the primitive turbulent variables k or ε . The coefficient $\varepsilon^{(2)}$ appearing in equation (19) is set to 8.0.

The gradient of the turbulent state vector is computed using the expression

$$\nabla \mathbf{Q}_j = \sum_{i \in E_j} \frac{\Delta s_{ij}}{2V_j} (\mathbf{Q}_i + \mathbf{Q}_j) \tag{20}$$

where Δs_{ij} is the area of the face shared by control volumes i and j and V_j is the volume of element j . The computation of the diffusive fluxes requires the evaluation of $\nabla \mathbf{Q}$ at the interfaces. To avoid spurious high frequency modes in diffusion-dominated regions, the diffusive fluxes are discretized according to

$$\nabla \mathbf{Q}_{ij} = \overline{\nabla \mathbf{Q}}_{ij} - \left[\overline{\nabla \mathbf{Q}}_{ij} \cdot \delta \mathbf{s}_{ij} - \frac{(\mathbf{Q}_i - \mathbf{Q}_j)}{|\mathbf{x}_i - \mathbf{x}_j|} \right] \delta \mathbf{s}_{ij} \tag{21}$$

$$\overline{\nabla \mathbf{Q}}_{ij} = \frac{1}{2} (\nabla \mathbf{Q}_i + \nabla \mathbf{Q}_j) \tag{22}$$

$$\delta \mathbf{s}_{ij} = \frac{\mathbf{x}_i - \mathbf{x}_j}{|\mathbf{x}_i - \mathbf{x}_j|} \tag{23}$$

which is analogous to the discretization of the mean flow equations as described in reference [14].

To avoid the need to resolve the high gradients near a no-slip boundary (solid wall), a high-Reynolds-number form of the turbulence model is employed. This requires a wall-matching procedure to be used to correct the mean flow gradients and turbulent quantities. To apply the wall-matching procedure, the log-law of the wall is used to derive three expressions that describe the wall shear stress, turbulence production term P_k , and the turbulence dissipation rate ε for near-wall grid models. The respective expressions for a node p located in

the log-law region are

$$\tau_w = \frac{(\rho u)_p C_\mu^{1/4} k_p^{1/2}}{1/\kappa_w \ln(E_w y_p^+)} \quad (24)$$

$$y_p^+ = \frac{y_p C_\mu^{1/4} k_p^{1/2}}{\nu} \quad (25)$$

$$\kappa_w = 0.41, \quad E_w = 9.0 \quad (26)$$

$$(P_k)_p = \tau_w \left[\frac{(\rho u)_p C_\mu^{1/2} k_p}{y_p \ln(E_w y_p^+)} \right] \quad (27)$$

$$\epsilon_p = \frac{C_\mu^{3/4} k_p^{3/2}}{\kappa_w y_p} \quad (28)$$

To apply this procedure in an unstructured algorithm that employs median dual control volumes, the wall shear stress for control volume faces lying above the boundary, as shown in Fig. 1, is computed using equation (24). The velocity u_p represents the wall-parallel component of the velocity vector at point p , and y_p is the orthogonal distance between point p and the wall. This computed shear stress is then resolved into x , y , and z components according to

$$\tau_{iw} = \tau_w \hat{u}_{ii}, \quad i = x, y, z \quad (29)$$

where \hat{u}_{ii} denotes the Cartesian components of the unit vector in the mean flow direction and tangent to the wall. Similarly, the production term P_k and the dissipation ϵ appearing in the source terms of the k - ϵ equations are computed in the corresponding control volumes using equations (27) and (28). For the dissipation equation, ϵ is explicitly specified at the grid nodes associated with near-wall control volumes according to equation (28), amounting to a Dirichlet boundary condition for the ϵ equation. A Neumann boundary condition is employed for the turbulent kinetic energy.

With the spatial discretization completed, a time-integration solution procedure is required to allow a stable, positive definite integration of the turbulence equations. To maintain consistency with the mean flow equations, a five-stage Runge–Kutta

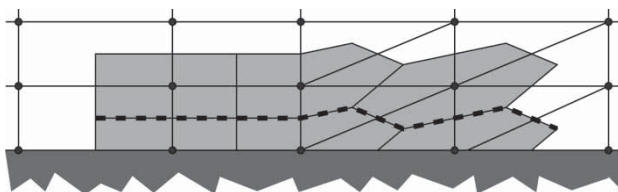


Fig. 1 Representation of median-dual control volume faces that are used for implementing the wall functions (shown with dashed line pattern)

scheme is used [4]. First, consider a single-stage scheme. This can be written as

$$\Delta \mathbf{Q}^n = -\Delta t R(\mathbf{Q})^n = -\Delta t (F'^C - F'^D - S') \quad (30)$$

where R is the residual operator of the system of turbulence equations and includes contributions from the convective fluxes (F'^C), diffusive fluxes (F'^D), and the source terms (S'). To stabilize the scheme, a point-implicit discretization of the source terms is employed to give

$$\begin{aligned} & \left[I - \Delta t \left(\frac{\partial S}{\partial \mathbf{Q}} \right) \right] \mathbf{Q}^{n+1} \\ & = \left\{ I - \Delta t \left[F'^C - F'^D - \left(S' - \frac{\partial S}{\partial \mathbf{Q}} \right) \right] \right\} \mathbf{Q}^n \end{aligned} \quad (31)$$

Spalart and Allamaras [20] showed that to guarantee positivity for such a scheme, the left-hand side matrix operator for the vector \mathbf{Q}^{n+1} must be a diagonally dominant matrix with positive diagonal elements and negative (or zero) off-diagonal elements. A key property of such a matrix is that its inverse contains only non-negative elements. In addition, they argued that a positive matrix operator is also required for the vector \mathbf{Q}^n on the right-hand side of equation (31). A positive matrix operator is one that when applied to a vector with non-negative elements will produce a vector with non-negative elements. Given these requirements, the source Jacobian ($\partial S/\partial \mathbf{Q}$) can now be chosen to ensure that the correct form of the matrix on the left-hand side results. In the current implementation, a diagonal Jacobian has been used. This choice decouples the two turbulence variable equations, thus simplifying the positivity analysis. To evaluate the Jacobian, the dissipation term in the turbulent kinetic energy equation is expressed in terms of k through the eddy viscosity relation (9). The resulting expressions for the negative part of the source terms are

$$S_k^- = -C_\mu \frac{\rho k^2}{\mu_t} - \max \left[0.0, \left(\frac{2}{3} \frac{\partial u_i}{\partial x_i} \rho k \right) \right] \quad (32)$$

$$S_\epsilon^- = -C_{\epsilon 2} \frac{\rho \epsilon^2}{k} - C_{\epsilon 1} \frac{\epsilon}{k} \max \left[0.0, \left(\frac{2}{3} \frac{\partial \mu_i}{\partial x_i} \rho k \right) \right] \quad (33)$$

Treating μ_t as a constant, the source Jacobian can thus be written as

$$\frac{\partial S}{\partial \mathbf{Q}} = \begin{bmatrix} \frac{\partial S}{\partial(\rho k)} & 0 \\ 0 & \frac{\partial S}{\partial(\rho \epsilon)} \end{bmatrix} \quad (34)$$

$$\frac{\partial S}{\partial(\rho k)} = -\frac{2\epsilon}{\rho k} - \max \left[0.0, \left(\frac{2}{3} \frac{\partial u_i}{\partial x_i} \right) \right] \quad (35)$$

$$\frac{\partial S}{\partial(\rho \epsilon)} = -2C_{\epsilon 2} \frac{\epsilon}{\rho k} - C_{\epsilon 1} \max \left[0.0, \left(\frac{2}{3} \frac{\partial u_i}{\partial x_i} \right) \right] \quad (36)$$

This particular choice of the source Jacobian provides no guarantee as to the positivity of the complete matrix operator on the right-hand side of equation (31). This is a result of the additional convective and diffusive flux contributions that are treated explicitly in the numerical scheme presented here, which can outweigh the stabilising effects of the point-implicit discretization of the source terms. To compensate for this explicit treatment of the fluxes, the source Jacobians are multiplied by an appropriately chosen scaling matrix \mathbf{Y} . In general, numerical problems can arise when $R'(\phi) > \partial S / \partial \phi$. The scaling matrix is, therefore, chosen to avoid this condition and produces a stronger under-relaxation of the turbulent equations. \mathbf{Y} is chosen to be a diagonal matrix whose elements are given by

$$\mathbf{Y}_\phi = \max \left\{ 1.0, \varepsilon^{(4)} \frac{-R'(\phi)^n}{[\partial S_\phi / \partial (\rho\phi)]^n} \right\} \quad (37)$$

$$\varepsilon^{(4)} = 1.5 \quad (38)$$

The arguments presented earlier are valid for a single-stage Runge–Kutta scheme. For a multi-stage scheme, the updates at each stage (l) are made with respect to the values at time step (n). The time integration for a multi-stage scheme is, therefore, modified to give

$$\begin{aligned} & \left[I - \alpha_l \Delta t \left(\mathbf{Y}^l \frac{\partial S}{\partial \mathbf{Q}} \right) \right] \mathbf{Q}^{l+1} \\ & = \left\{ I - \alpha_l \Delta t \left[F^{rC} - F^{rD} - \left(S' - \mathbf{Y}^l \frac{\partial S}{\partial \mathbf{Q}} \right) \right] \mathbf{Q}_r \right\} \mathbf{Q}^n \end{aligned} \quad (39)$$

$$\mathbf{Q}_r = \begin{bmatrix} \frac{(\rho k)^l}{(\rho k)^n} & 0 \\ 0 & \frac{(\rho \varepsilon)^l}{(\rho \varepsilon)^n} \end{bmatrix} \quad (40)$$

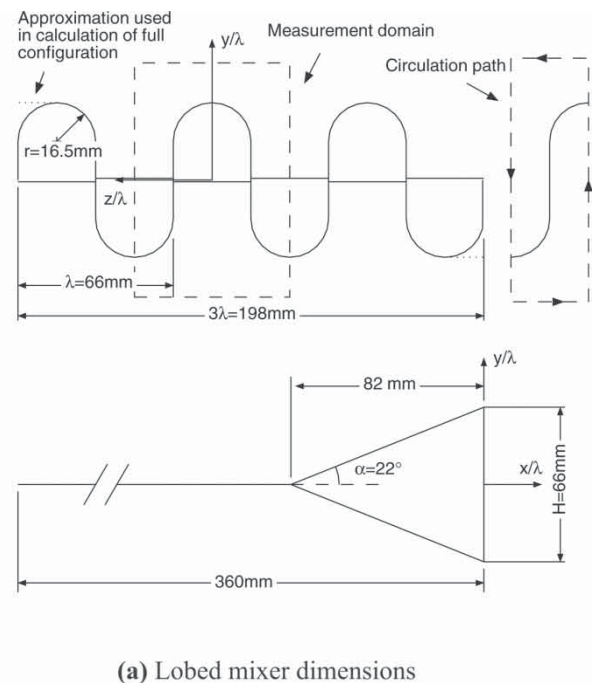
The time step Δt used to integrate the two turbulence equations is computed from the stability considerations of the convective and the diffusive fluxes. Further details can be found in reference [4].

4 MIXER CONFIGURATIONS

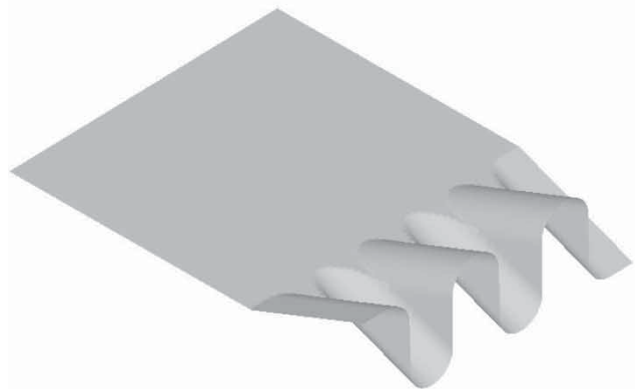
Two separate mixer configurations have been chosen to perform the simulations presented. The first is a simplified (spanwise straightened) coplanar mixer configuration based on the experimental configuration of Yu and Yip [8], which has also been modelled by Salman *et al.* [7] using an incompressible Navier–Stokes multi-block structured grid algorithm. Details of this mixer definition are

given in Fig. 2. To reduce the problem size and to simplify the computations carried out here, a spanwise periodic flow structure is assumed within the mixing region. This simplification implies the presence of planes of symmetry between adjacent streamwise vortices such that only half a lobe need be modelled. This is in contrast to the predictions of reference [6], which considered the full mixer configuration.

The computations presented subsequently for this mixer were carried out with the inlet boundary condition as used in the incompressible structured algorithm predictions of Salman *et al.* [7], corresponding to the experimental conditions of the Yu and Yip [8], data. The two streams were set at



(a) Lobed mixer dimensions



(b) Solid CAD model

Fig. 2 Definition of mixer configuration of Yu and Yip [8]

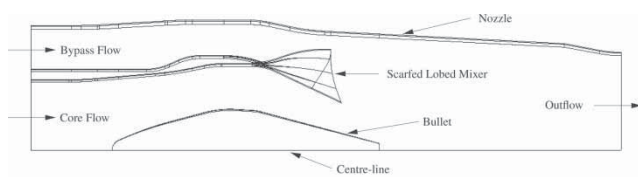
a static pressure and density ratio of 1.0. The axial velocities were set to 6 ms^{-1} (u_{low}) in the slow (upper) stream and 10 ms^{-1} (u_{high}) in the fast (lower) stream, corresponding to Mach numbers of 0.0176 and 0.0294, respectively, as were used in the low-speed experiments of Yu and Yip [8]. The inlet boundary conditions for the turbulence quantities were evaluated on the basis of a turbulence intensity of 1 per cent, matching that reported by the experimentalists, and an eddy viscosity equal to the molecular viscosity. At inlet, spatially uniform profiles were assumed. The top and bottom tunnel walls were modelled as slip walls, but on the mixer surface, a no-slip condition was used. Owing to the low velocities encountered for this case, the low Mach number preconditioner of the unstructured algorithm was employed. Further details of the low Mach number preconditioner can be found in reference [15].

The second mixer configuration computed is a lobed mixer geometry with scarfing, as typically found in modern engine representative applications. An outline and a solid CAD model of this mixer are shown in Fig. 3. The outline illustrates the overall flow configuration together with the key components that define the flow domain, namely, a central bullet, the mixer, and the mixing duct (nozzle) outer wall. The solid CAD model shows just two of these components: the lobed mixer surface definition and the bullet located on the centre-line. This mixer configuration consists of six long lobe gullies and six short gullies alternating circumferentially. The scarfing introduced at the trailing edge of the lobes is clearly seen on this three-dimensional CAD

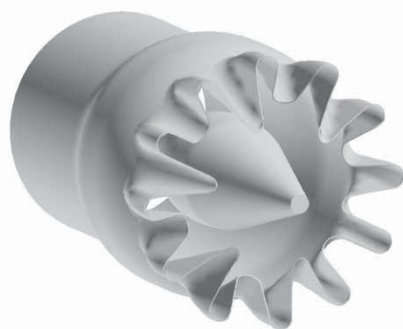
model. Owing to the introduction of the scarfing, the circumferential periodicity in this mixer is now equivalent to one complete lobe wavelength of an equivalent non-scarfed mixer. As there is no swirl in the flow, symmetry boundary conditions can be utilized and only half of one lobe wavelength needs to be modelled. The modelled sector encompasses half a short lobe gully and half a long lobe gully.

The scarfing introduced to the lobed mixer surfaces raises difficulties in unambiguously defining certain geometrical parameters associated with the lobes. Referring to the side view of the lobe surface in Fig. 3(a), it is notable that a clear definition of the mixer height is not at all obvious. The definition adopted here has been based on an effective lobe height (H_{eff}). This is defined as the corresponding height of a non-scarfed mixer in which the trailing edge lies on the same plane as the lobe peak of the scarfed mixer. Using this definition, the effective lobe height is $H_{\text{eff}} = 0.0452 \text{ m}$. The inlet plane was located $6.5H_{\text{eff}}$ upstream of the lobed mixer trailing edge, whereas the exit plane of the mixing duct was at a distance $6.3H_{\text{eff}}$ downstream of the mixer trailing edge. At the exit plane, the diameter of the nozzle was equal to $4.29H_{\text{eff}}$.

This mixer configuration was recently the subject of a detailed experimental study [10], in which temperature measurements were made downstream of the lobed mixer within the mixing duct. The test conditions used in these experiments are tabulated in Table 1. These conditions were employed in the numerical simulations performed on this mixer. The inlet turbulence levels were taken to be 3 per cent of the local inlet velocities and the value of ϵ was fixed on the basis of an eddy viscosity equal to ten times the molecular viscosity, and it was checked that this produced a realistic turbulence length scale. Tests showed that the strong generation of turbulence in the shear layers makes these types of problems relatively insensitive to inlet turbulence conditions. The mixer, bullet, and nozzle boundaries were all simulated as no-slip wall boundaries. At the inlet, the Mach number of the bypass and core flows were 0.42 and 0.41 corresponding to velocities of 155.22 and 229.67 ms^{-1} , respectively. The Mach number at exit was equal to 0.83 corresponding to a mixed out velocity of 326.54 ms^{-1} .



(a) Outline of lobed mixer, nozzle, and bullet



(b) Solid CAD model

Fig. 3 Realistic mixer configuration

Table 1 Experimental test conditions used for model of scarfed mixer

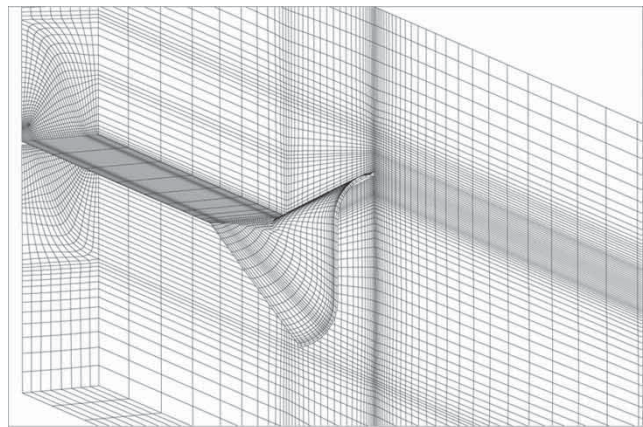
Properties	$\left(\frac{P_{\text{total}}}{P_{\text{ambient}}}\right)$	Total temperature (K)	Ambient pressure (kPa)	Ambient temperature (K)
Bypass flow	1.6418	346.0	102.487	278.1
Core flow	1.5474	795.4	102.487	278.1

5 GRID GENERATION

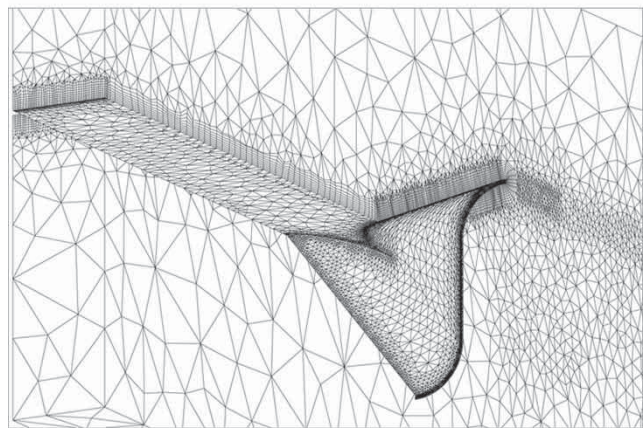
Three mesh types were employed for the mixer configuration of Yu and Yip [8], to study the influence of mesh type on lobed mixer predictions. The grids employed include a hexahedral grid, a tetrahedral grid, and a mixed grid. All grids were generated for a half lobe wavelength as described earlier, in order to reduce the problem size. An important factor that needs to be considered when comparing solutions across different mesh types is the number of unknowns being compared. Structured hexahedral grids tend to have a comparable number of cells and nodes, whereas three-dimensional unstructured tetrahedral grids contain five to six times as many cells as there are nodes in a given mesh. The number of unknowns will, therefore, be very different depending on whether a cell-centred or a cell-vertex scheme is being employed. The unstructured algorithm used here is a cell-vertex method that stores unknowns at the nodes of the primal grid. It is important, therefore, to compare solutions across different grid types that consist of the same number of nodes. In the current work, all three grids generated for the study regarding the influence of different mesh types for lobed mixer flows contained approximately 150 000 nodes.

The hexahedral grid generated with the software ICM Hexa is shown in Fig. 4(a). This grid in fact consists of a multi-block structured grid topology containing seven blocks with matching nodes between adjacent blocks at the interfaces. The benefits of this topology are the improved grid orthogonality within the mixing region and the ability to capture the mixer surface with a body-fitted grid. Further upstream, the grid orthogonality is sacrificed but the flow there is predominantly uniform and inviscid. Hexahedral elements allow highly stretched elements to be used without deterioration of solution quality. This feature is employed in the streamwise direction where high grid resolution is not required as axial gradients were generally smaller than gradients transverse to the mixing layer. An obvious deficiency of this mesh type is the inefficient clustering of node (e.g. wasted elements in the upstream region where the flow is essentially uniform).

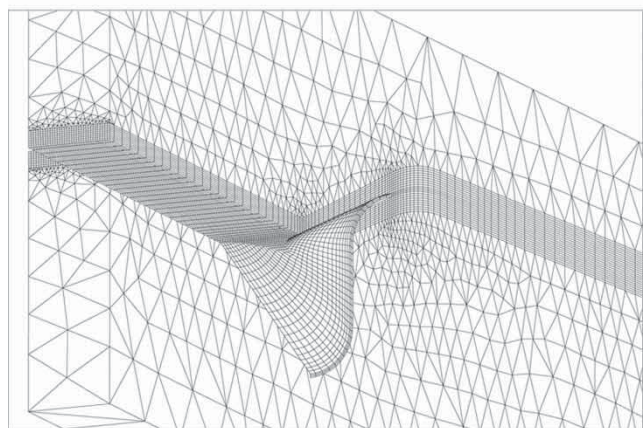
The second meshing strategy employing a fully automated process for generating the lobed mixer grid is shown in Fig. 4(b). The grid consists of two element types: prism elements and tetrahedral elements. This approach allows the mixer geometry to be captured easily and has the potential of being easily extended to more complex mixers. A structured layer of prism elements is generated normal to the mixer surface to resolve the boundary layer efficiently. Tetrahedral elements are then used to fill the remainder of the computational domain.



(a) Hexahedral grid



(b) Tetrahedral grid



(c) Mixed grid

Fig. 4 Grids for mixer configuration of Yu and Yip

Unlike the hexahedral grid, this approach provides a significant computational saving upstream of the mixer where the flow is uniform and a much coarser grid can be used. However, efficient resolution of the boundary layer requires highly stretched elements in the streamwise direction. As prism elements are

generated from triangular elements on the surface, anisotropic triangular elements are, therefore, unavoidable. Additionally, a layer of highly stretched tetrahedra joining the prisms would need to be generated. Generating such highly stretched elements with the software used (ICEM Tetra) presented problems. This limitation resulted in less efficient resolution of the boundary layers with this grid. In the present study, this grid is simply referred to as the tetrahedral grid because only tetrahedral elements were used within the free shear layer mixing region where the focus of interest lies for the current work.

The third mesh type employed hexahedral, tetrahedral, and pyramidal elements and is shown in Fig. 4(c). This meshing strategy provides an intermediate approach, semi-automating the grid generation, but allowing control of the hexahedral parts of the grid. In principal, such an approach should combine the advantages of both the first two strategies. Tetrahedral grids are used in the inviscid parts of the flow where the flow gradients are much smaller and alignment of the grid with the flow is not required. In regions where viscous and turbulent effects are important, such as in boundary and shear layers, hexahedral grids are used. The ability to generate stretched hexahedral elements that do not deteriorate solution quality should allow these flow features to be resolved more efficiently than with a tetrahedral grid. The two mesh types are then joined together at the interface through transition pyramidal elements. In practice, one finds difficulties in using very highly stretched hexahedral grids. Such grids cause pyramidal elements with highly skewed surfaces to be generated. Problems consequently arise in generating the tetrahedral grids at the interface with the pyramidal elements. To remedy this difficulty, the grid resolution in the streamwise direction was increased slightly to reduce the aspect ratios of the quadrilateral faces, which form the bases of the pyramidal elements. This modification allowed the grid to be completed successfully with the grid generation software ICEM Tetra and ICEM Hexa. As pointed out earlier, high grid resolution is required primarily in a direction normal to the shear layer. For brevity, in the text that follows, this grid will simply be referred to as the mixed grid.

Motivated by the numerical results to be presented subsequently, in which the influence of different mesh types on the prediction of lobed mixer flow was assessed, a purely hexahedral grid consisting of 550 000 nodes was used to discretize the computational domain of the scarfed mixer geometry. The primary problem with the use of hexahedral grids is related to the skewed end plane of the lobed mixer scarfing which complicates the grid generation

process further. It was decided that a grid topology similar to the one used for the non-scarfed (coplanar) mixer configurations studied by Salman *et al.* [7] should be employed. This allowed the grids shown in Figs 5(a) and (b) to be generated, consisting of a nine-block topology. The figures show that the lobed mixer surface is very well represented, despite the addition of the scarfing. The main effect of the scarfing on the generated grid is seen on the curvilinear surface in Figs 5(a) and (b). The whole surface is distorted. This is in contrast to the equivalent surface in a coplanar mixer in which the surface lies on a plane perpendicular to the streamwise direction. The distortion of this surface increases near the scarfed mixer trailing edge. A feature that raised particular

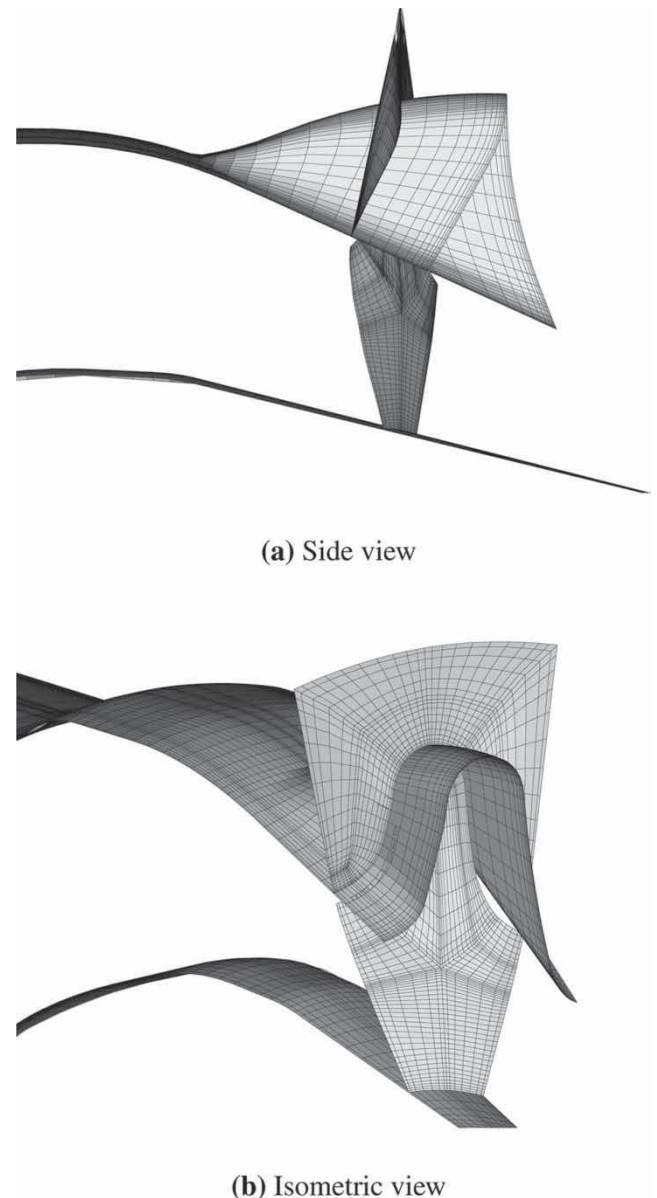


Fig. 5 Hexahedral grid for realistic scarfed mixer configuration

problems was the cusped trailing edge of the long lobe gully, which introduced severe skewness in the generated hexahedral grids. Adopting careful nodal distributions and smoothing strategies in the vicinity of this region allowed acceptable grids to be generated.

To clarify the nature of the grid topology and the nodal distribution for this complex mixer configuration, cross-sectional grids are presented in Fig. 6. The four cross-sections were generated at locations corresponding to (a) the inlet plane, (b) a plane bisecting the length of the lobed mixer, (c) the lobed mixer scarfed trailing edge, and (d) at a location $x/H_{eff} = 1.58$ within the mixing duct. In planes (b) and (c), the grids do not extend to the centre-line because of the presence of the bullet. In plane (c), the asymmetric grid is evident in the vicinity of the scarfed lobed mixer trailing edge. The four locations shown clearly illustrate the good grid quality achieved throughout the computational domain for this challenging geometry of a scarfed mixer configuration.

6 RESULTS

The basic unstructured mesh code used in references [14, 15] did not contain a two-equation turbulence model; hence, to verify the implementation of the $k-\epsilon$ model in the code which is conducted as part of the present work, two test cases were first predicted corresponding to a near-wall turbulent shear layer and a free turbulent shear layer.

6.1 Developing boundary layer

An incompressible spatially developing two-dimensional boundary layer was simulated to verify the implementation of the high-Reynolds-number model and wall functions. The zero pressure gradient boundary layer can be defined by a thickness parameter, usually taken to be the momentum thickness Reynolds number $Re_\theta = u_e \theta / \nu$, where u_e is the velocity near the edge of the boundary layer. Bardina *et al.* [21] performed detailed computations of this flow providing comparisons of various parameters, including the variation of the skin friction coefficient C_f with Re_θ . The current work attempts to reproduce these predictions with the standard $k-\epsilon$ model used here. The tests help to verify the discretization employed and to compare the predicted results observed with both structured [7] and unstructured algorithms [15].

The computations presented used a constant velocity of 10 ms^{-1} at inlet. Inlet turbulence intensity was set at 1 per cent and ϵ was based on an assumed eddy viscosity at inlet of 10μ . The bottom wall was set to a no-slip boundary, whereas a slip wall was assumed for the far-removed top boundary. Following the guidelines provided by Bardina *et al.* [21], the computational grid consisted of 125 nodes non-uniformly distributed in the streamwise direction and 124 nodes in the cross-stream direction.

Mean velocity profiles at $Re_\theta = 100\,000$ are shown in Fig. 7, together with the data taken from Bardina *et al.* for Coles' law [22]. The results indicate that the log-law behaviour is well captured with all the simulations carried out in good agreement with Coles' correlation. For comparison, the velocity

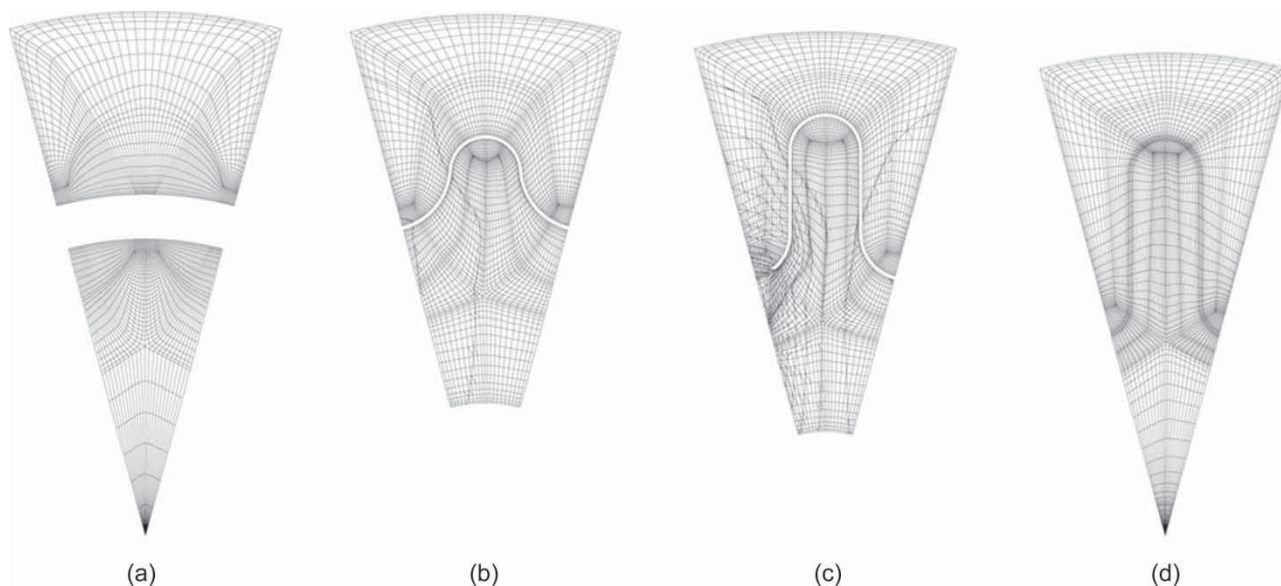
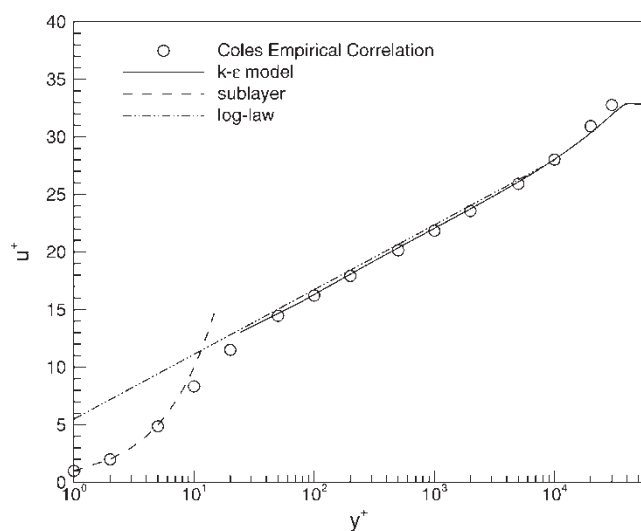
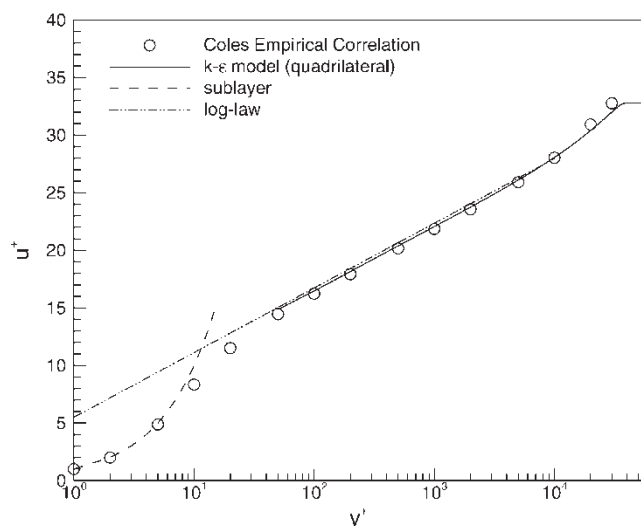


Fig. 6 Cross-sectional planes of mesh generated for the realistic mixer configuration



(a) Structured algorithm



(b) Unstructured algorithm

Fig. 7 Predictions of turbulent boundary layer velocity profile

profiles computed using the structured algorithm used by Salman *et al.* [7] have also been included. With the structured algorithm, the velocity profile is captured from $y^+ \approx 30$. This value is around 50 for the results computed with the unstructured algorithm. The difference reflects the additional distance introduced by the half control volumes that arise in the near-wall median dual control volumes as seen in Fig. 1. Nevertheless, both algorithms produce results in close agreement. Figure 8 shows comparisons with Coles' C_f correlation for the variation of skin coefficient with Re_θ . Generally, results for the skin friction coefficient are in very good agreement in both cases. The results presented show that the correct near-wall behaviour is reproduced. This

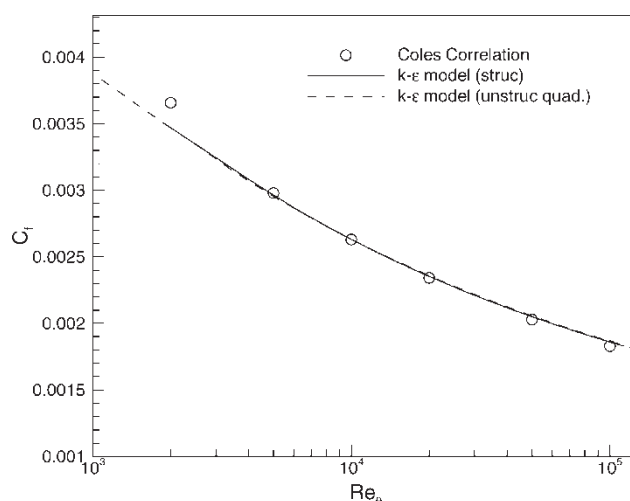


Fig. 8 Variations of skin friction coefficient and shape factor with Reynolds number

confirms the correct implementation of the high Reynolds number $k-\epsilon$ turbulence model and associated wall functions.

6.2 Planar-free shear layer

The free turbulent mixing layer is defined as the region between two parallel streams moving at different speeds. This flow is a simplification of the convoluted shear layers that are produced by lobed mixers and was considered a fundamental test case in the development of turbulence models. This flow, therefore, provides an important test case in the prediction of lobed mixer flows.

An important property of the planar-free shear layer is the concept of self-similarity, which the flow attains at sufficiently large Reynolds numbers and downstream distance. Under these conditions, the mean and turbulence quantities at different streamwise locations assume profiles, which, when scaled with the local shear layer thickness, have the same shape. This self-preserving behaviour is associated with a linear growth of the planar mixing layer. The behaviour can be correctly predicted only if the correct physical mixing rate is simulated. The spreading rate parameter can, therefore, be used as a quantitative measure of the level of mixing being predicted. Together with the ability to predict the mean velocity profile correctly, these are considered the most significant parameters in this flow. Comparisons presented will, therefore, concentrate on these two aspects.

The experimental data presented below have been taken from Liepmann and Laufer [23]. These experimental data were also used by Bardina *et al.* [21], who carried out a computational study of the

incompressible planar mixing layer with several turbulence models, including the Launder–Sharma low-Reynolds-number $k-\varepsilon$ model [24]. In deriving the predicted spreading rates, the mixing layer thickness, d_{layer} , was defined as the distance between points in the mean velocity profile where the square of the non-dimensional mean velocity is 0.1 and 0.9, respectively. The non-dimensional mean velocity is given by

$$U^* = \frac{u - u_{\text{low}}}{u_{\text{high}} - u_{\text{low}}} \quad (41)$$

where u_{low} and u_{high} are the velocities of the low- and high-speed streams. The mean velocity profiles are plotted in terms of U^* and the transverse distance similarity parameter (η) is given by

$$\eta = \frac{2(y - d_{\text{ave}})}{d_{\text{layer}}} \quad (42)$$

where d_{ave} is the position of the centre of the shear layer defined as the point where $u = (u_{\text{low}} + u_{\text{high}})/2$. It should be noted that, in general, $d_{\text{ave}} \neq 0$ for free shear layers, which often exhibits a skewing such that the centre-line is tilted towards the slow stream [25].

The results presented have been obtained with a $4 \text{ m} \times 4 \text{ m}$ computational domain. At inlet, the flow conditions were 6 ms^{-1} for the slow stream and 10 ms^{-1} for the fast stream, corresponding to Mach numbers of 0.0176 and 0.0294, respectively, which again necessitated the use of the low Mach number preconditioner [15]. The static pressure and density ratios of the two streams were set to unity. Slip walls were imposed on the top and bottom boundaries of the domain, located at equal distances (2 m) from the mixing layer. The inlet turbulent kinetic energy was specified by assuming a turbulence intensity (ti) of 1 per cent of the local free stream velocity (u_∞). The inlet turbulence dissipation ε was set on the basis of an eddy viscosity equal to 10μ . The computational grid used consisted of quadrilateral elements with a resolution of 64×64 elements.

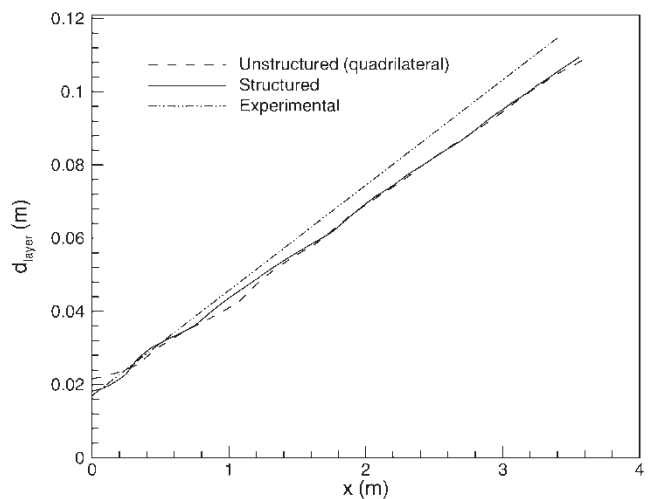
The experimental data of Liepmann and Laufer were taken for a mixing layer in which one stream was at rest. Townsend [26] has derived an expression that relates velocity ratio with the mixing layer spreading rate

$$\left(\frac{u_{\text{high}} + u_{\text{low}}}{u_{\text{high}} - u_{\text{low}}} \right) \frac{dd_{\text{layer}}}{dx} = \text{constant} \quad (43)$$

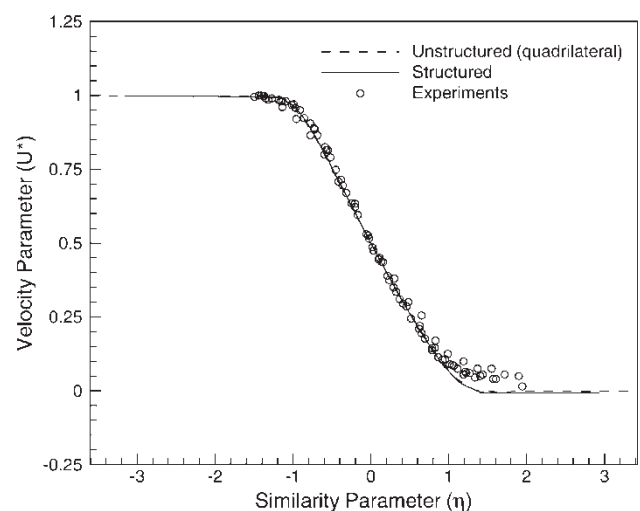
This scaling was used to allow the experimental data taken from Liepmann and Laufer to be compared with the present simulations.

Profiles of the predicted spreading rates are shown in Fig. 9(a), labelled as ‘unstructured quadrilateral’ predictions. For comparison, the spreading rate obtained from the structured algorithm of Salman *et al.* [7] has also been included. The predictions obtained with the two algorithms are essentially identical. The linear self-similar spreading rate predicted by both algorithms is 0.0245. This is in agreement with the values quoted by Wilcox [27]. The experimental value of 0.02875 derived from the data of Liepmann and Laufer is also included. This experimental value is quoted with an uncertainty of about ± 10 per cent.

With the self-similar spreading behaviour demonstrated, the velocity profile taken at a streamwise location of $x = 3.5 \text{ m}$ has been plotted in Fig. 9(b),



(a) Shear layer spreading



(b) Shear layer velocity profile

Fig. 9 Comparison of predicted shear layer properties with experiments

together with experimental data derived from Liepmann and Laufer. Comparison of the velocity profiles predicted by the two algorithms reveals essentially identical predictions. The good agreement with the measurements demonstrates again that the self-similar behaviour has been captured and completes the verification of the model implementation for free shear flows.

The planar shear layer flow was now used as a testbed for assessing the influence of a variety of grid types on the accuracy of flow predictions of free shear layers. Studying the sensitivity to the grid of the predicted shear layers in this simplified flow helps understand some of the underlying numerical issues in modelling lobed mixer complex shear layers. This illustrates the impact of using unstructured tetrahedral grids, predicting the convoluted mixing layers arising in these flows accurately. Computations for the planar shear layer were repeated on the three grid types as shown in Fig. 10. These included a purely quadrilateral mesh, three triangular meshes, and a mixed mesh. Three of these grids (Figs 10(a) to (c)) contained the same

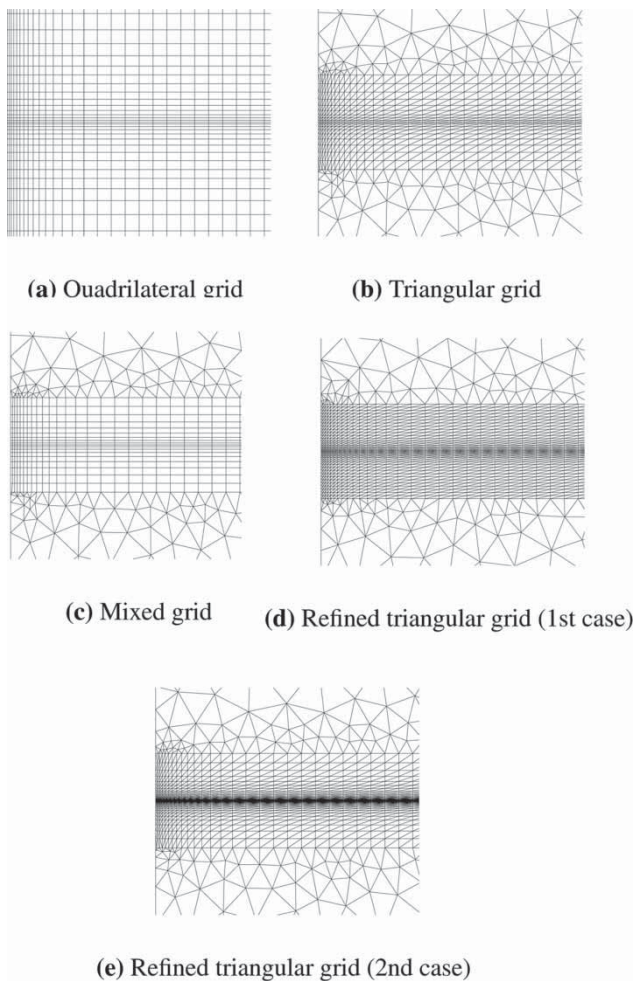
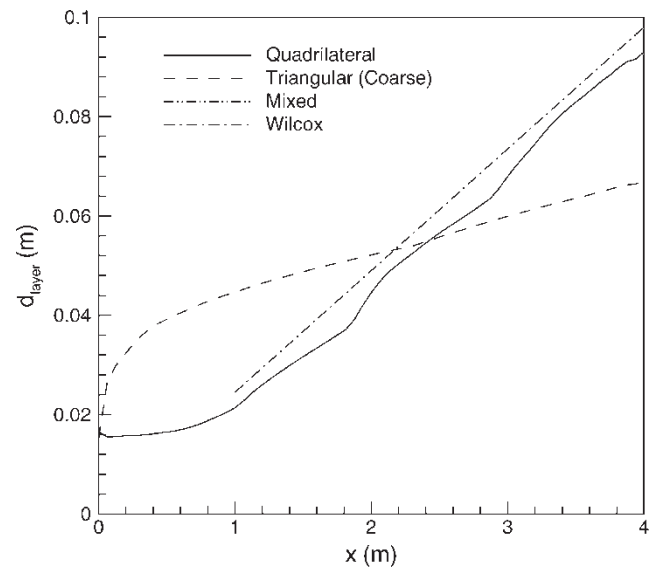


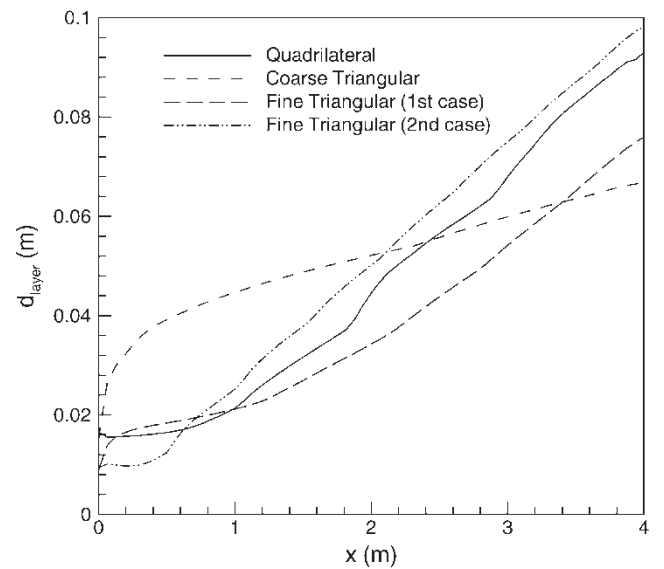
Fig. 10 Planar shear layer grids at the inlet boundary

nodal distribution within the shear layer region. The nodal distribution was modified for the last two grids shown in Fig. 10 for the reasons described subsequently. Note that the same three meshing strategies that were presented in section 5 for the convoluted shear layer in the Yu and Yip lobed mixer have been initially studied here for the simple two-dimensional planar case.

Figure 11(a) presents the predicted spreading rate of the mixing layer for grids (a), (b), and (c). A reference $k-\epsilon$ result for the self-similar spreading rate



(a) Comparison of different grid types



(b) Comparison of triangular grids

Fig. 11 Variation of shear layer thickness with downstream distance

taken from reference [27] has also been included. Results for the quadrilateral grid (a) reveal the correct spreading has been obtained, even though it contains just eight nodes across the mixing layer by $x = 4$ m. The triangular mesh (b) of similar density shows a very different behaviour. A very rapid growth of the shear layer within the first 1 m is observed. The spreading then decreases rapidly such that it is ~ 40 per cent of the correct spreading rate by $x = 2$ m. The mixed grid result is identical to the quad mesh result. The meshes are identical in the shear layer region, but the mixed grid has a poorer quality and coarser mesh in the outer regions. This result shows that the mesh quality in the outer region has little effect.

To identify the reasons for these results, two aspects of the discretization are considered. First, differences in control volumes between the triangular and quadrilateral grids associated with cells lying within the shear layer are shown in Fig. 12. Additionally, recall from section 3 that the inviscid fluxes include a smoothing term on the basis of the one-dimensional decomposition along the grid edges. This one-dimensional decomposition is performed essentially in a direction transverse to the control volume faces. In this shear layer flow, the Cartesian transverse component of velocity is much smaller than the Cartesian or streamwise component. Therefore, the flow is more or less aligned with the horizontal finite volume faces and normal to the vertical faces. The numerical smoothing, which results from the quadrilateral grid, is thus very small. For control volume disposition relative to the dominant flow direction as in the triangular grid, as shown in Fig. 12, control volume faces exist whose transverse direction is oblique to the main flow direction. When performing the one-dimensional decomposition into the characteristic variables on such faces, a significant velocity component will arise in the direction, resulting in higher numerical smoothing than in the quadrilateral grid. This accounts for the higher spreading occurring in the early stages of the shear

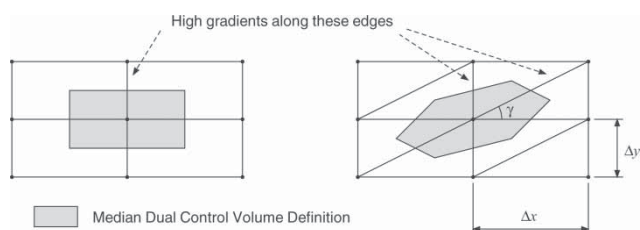


Fig. 12 Form of control volumes within the shear layer region obtained by using quadrilateral and triangular grids

layer, as indicated in Fig. 11(a). The increased spreading reduces velocity gradients across the layer, resulting in lower production of turbulent energy and hence lower eddy viscosity. The rapid decrease in spreading rate that follows is a direct consequence of this drop in turbulent energy and eddy viscosity.

The arguments presented earlier suggest that reducing the angle (γ) defined in Fig. 12, such that the oblique control volume faces become more aligned with the flow, would reduce the effects of the numerical smoothing. This can be achieved by either increasing the grid spacing (Δx) in the streamwise direction or reducing the cell height (Δy). Calculations for triangular grids were, therefore, repeated with two more cases. First, the grid resolution across the shear layer was doubled (Fig. 10(d)). Predictions for this case are shown in Fig. 11(b), together with the quadrilateral and coarse triangular grid solutions. A much lower spreading is evident in the early stages. Further downstream, the flow is able to recover reaching the expected self-similar behaviour. The problems encountered in the early stages are associated with the low aspect ratio ($\Delta x/\Delta y$) cells present in this region. A second refined grid was, therefore, studied, which consisted of an equal number of nodes as in Fig. 10(d), but with nodes redistributed across the shear layer to increase the aspect ratios of cells at the inlet (Fig. 10(e)). The shear layer spreading for this case is also shown in Fig. 11(b) and clearly demonstrates the reduced numerical smoothing which results.

Unstructured triangular grids clearly have an advantage in providing more efficient clustering of the grid. However, this simple study has demonstrated the superiority of quadrilateral elements in terms of solution accuracy when shear layer spreading is critical and the shear layer is disposed at an angle to unstructured mesh edges. These findings motivate a mixed grid approach for tackling the shear layer problem. An example of a prediction using a mixed quadrilateral/triangular grid is included in Fig. 11(a), corresponding to the mesh shown in Fig. 10(c). The grid consisted of 1531 nodes, compared with the 2880 nodes found in the quadrilateral grid. The spreading rate coincides with the solution from the quadrilateral grid. This occurs as the shear layer remains within the quadrilateral part of the grid throughout the length of the solution domain, although the triangular mesh in the outer inviscid regions has allowed a smaller (i.e. cheaper) mesh to produce the same predictive accuracy. The solution quality clearly illustrates the potential for such an approach to produce high quality numerical solutions at reduced computational cost.

6.3 Simplified coplanar lobed mixer flow field

The sensitivity of the predicted spreading rate of the planar shear layer to different grid types suggests that automatically generated unstructured grids might not necessarily be well suited for predicting lobed mixer convoluted shear layers. Although the simple planar shear layer flow has highlighted the primary causes behind the observed numerical behaviour, the subsequent implications for general lobed mixer shear layers of using unstructured tetrahedral grids remain unclear. It was decided that only by performing and analysing the computations of lobed mixer flows can the precise magnitude of these numerical effects be identified. In this section, the consequences of the numerical issues raised earlier regarding the use of tetrahedral grids for predicting convoluted shear layers are examined. In particular, the generation of high aspect ratio tetrahedral elements is not easily achievable and thus the accuracy of solutions for the three grid strategies for lobed mixer geometry presented earlier is now addressed.

Results for the three lobed mixer grids will be compared in detail in the near field of the coplanar mixer ($0 - 3H$). Figure 13 presents the results obtained at four axial planes for the three different grids. Results are presented in terms of streamwise velocity contours normalized with the velocity difference between the two streams (Δu). The corresponding cross-sectional grids at each location are also shown. Figures 13(a) to (d) illustrate the downstream evolution of the shear layer form of the lobed mixer trailing edge for the purely hexahedral grid. Results for the purely tetrahedral grid are presented in Figs 13(e) to (h). Beginning at location $x/H = 0.25$, the grid is clearly seen to be finely clustered along the mixer trailing edge in both meshes. Already at this location, the velocity contours exhibit a noticeably different distribution within the shear layer in Fig. 13(a). In particular, the low velocity contours ($u/\Delta u < 1.25$) in Figs 13(e) to (h) have been smoothed out significantly. These contours are associated with the boundary layers on the mixer's surface. The higher level of smoothing in the tetrahedral grid has contributed to the smearing of the high gradient region. Another significant difference seen at the first active location is near the lobe trough on the low-speed flow side, indicating a stronger rotation of the shear layer in comparison with the hexahedral results. Further downstream, the tetrahedral grid is gradually coarsened as seen in Figs 13(f) to (h) to allow a similar number of nodes to be used in all the cases studied. The resulting effect on the shear layer is higher numerical diffusion, evident from the higher spreading of the shear layer. Additionally, owing the convoluted shape of the

shear layer, it is not possible to distribute nodes efficiently as the shear layer no longer lies along a region identified readily with the mixer trailing edge geometry. An increase in numerical smoothing is noticed as the shear layer moves into relatively coarse parts of the grid. An example of this is seen at location $x/H = 1.0$ in Fig. 13(f), where a small part of the shear layer remains aligned with the vertical mixer walls. This portion is clearly less diffused than those parts of the shear layer that have migrated further out into the coarser regions of the grid, particularly when compared with the hexahedral solution. An important feature to note in Fig. 13(f) is the strong 'kink' in the shear layer when compared with corresponding results from the hexahedral grid. This implies that the streamwise vorticity responsible for rotation is stronger than in the hexahedral case, despite the higher level of numerical smoothing present. This behaviour is associated with a higher 'spurious' vorticity field, which can arise in tetrahedral grids as described in reference [4]. Numerical smoothing continues further downstream to cause the shear layer to become highly smeared in the purely tetrahedral grid by $x/H = 3.0$ when compared with the hexahedral solution.

The results presented so far are reminiscent of the numerical issues encountered in the study of the two-dimensional planar shear layer. In that study, the mixed grid provided the best approach in terms of solution accuracy and computational cost. Results for the mixed grid for the coplanar lobed mixer are shown in Figs 13(i) to (l). Generally, the results for this grid configuration are in much better agreement with the purely hexahedral results. Although the shear layer remains in the hexahedral part of the grid (e.g. at $x/H = 0.25$ and $x/H = 1.0$), the shear layer structure is seen to be very similar to that in Figs 13(a) to (d). The level of shear layer movement is essentially identical in both the hexahedral and mixed grids. Further downstream, the shear layer remains very well captured with higher numerical diffusion occurring only locally, mainly in the tetrahedral regions. Only by adopting an adaptive meshing algorithm can the convoluted shear layer be guaranteed to be always contained within the hexahedral grid region. This capability, however, was not available in the algorithm employed here. A purely hexahedral grid strategy was, therefore, the optimum for yielding the accurate numerical predictions of three-dimensional complex shear layers.

6.4 Scarfed lobed mixer flow field

Given the conclusions reached in the grid dependence studies discussed, numerical results for the scarfed mixer were computed using the hexahedral

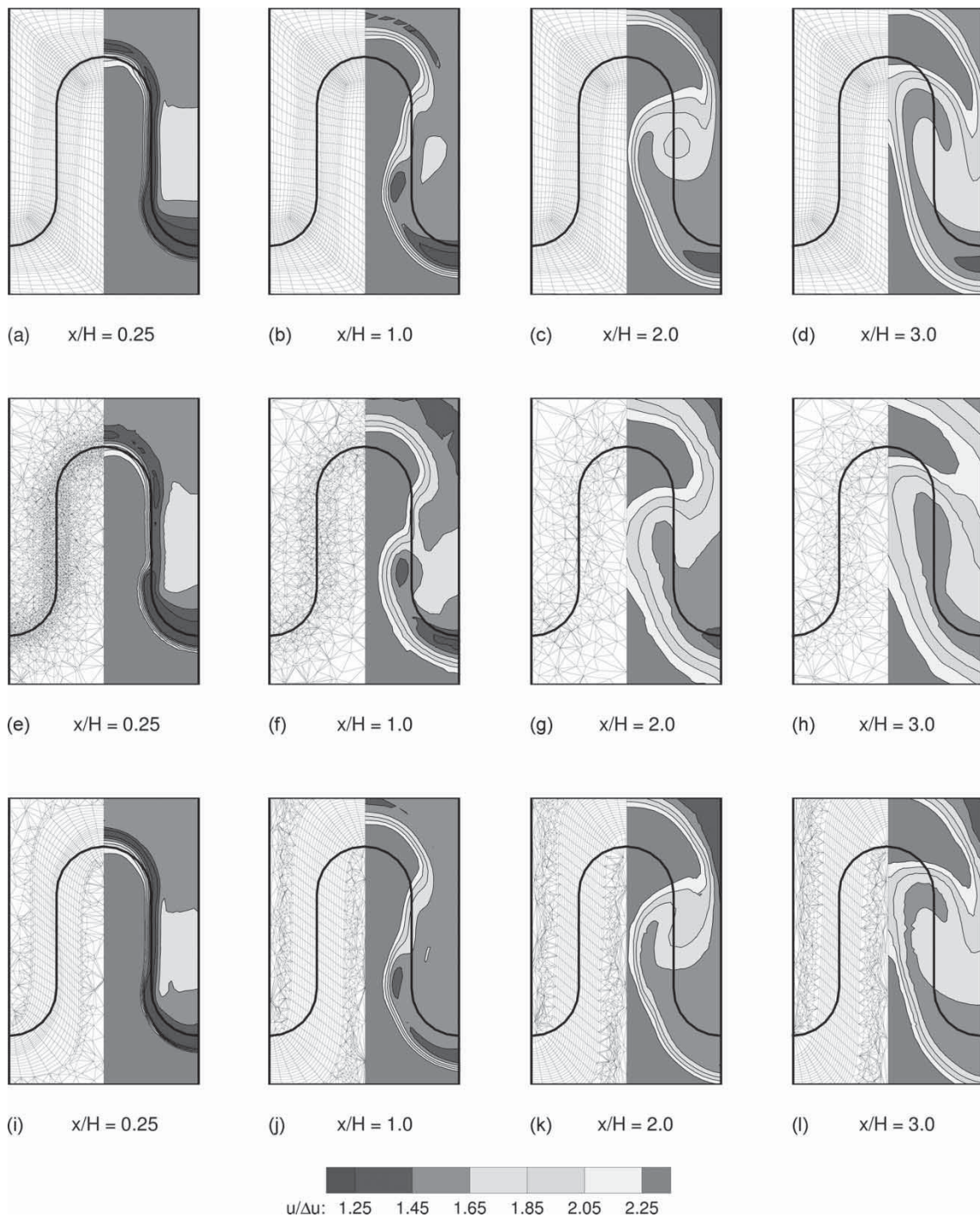


Fig. 13 Normalized streamwise velocity contours with cross-sectional grids at corresponding locations: (a) to (d) hexahedral grid, (e) to (h) tetrahedral grid, and (i) to (l) mixed grid

gridding strategy presented in section 5. Predicted Mach number contours at three streamwise locations downstream of the lobe peak at the mixer trailing edge are shown in Fig. 14. At $x/H_{\text{eff}} = 1.0$, the contours show that a low subsonic flow exists throughout the entire cross-section with the free stream values in the bypass (upper) and core (lower) streams equal to 0.5 and 0.4, respectively.

The higher Mach number in the bypass flow is a consequence of the high temperature difference between the two speeds, thus resulting in a higher speed of sound in the core flow.

The Mach number contours around the trailing edge of the mixer show an asymmetric distribution, a result of the scarfing introduced into the lobes. The distributions indicate that the strongest

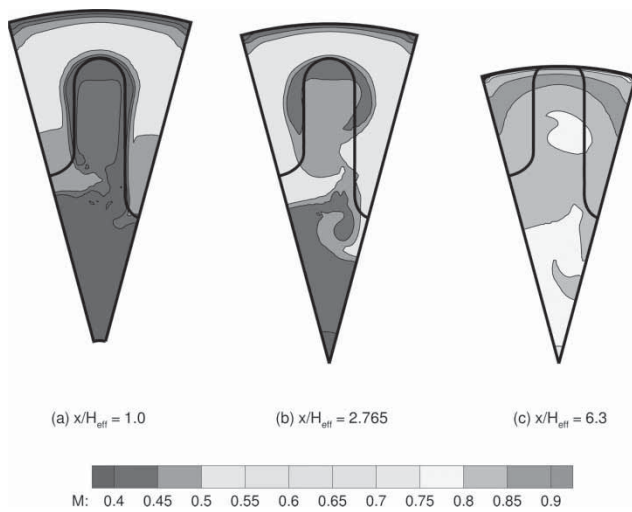


Fig. 14 Mach number contours

distortions occur closer to the lobe troughs. Near the lobe peak, very little evidence of the distortion of the shear layer is present. Adjacent to the outer wall (nozzle) surface, a region of low Mach number is captured, reflecting the formation of boundary layers on the nozzle wall. At $x/H_{\text{eff}} = 2.765$, the strong gradients observed at the previous location near the lobe troughs lead to the breakup of the contours into two separate regions. An 'island' of low Mach number fluid now exists in the vicinity of the lobe peak. The structure is somewhat more rounded than at the previous location and protrudes further into the bypass stream, reflecting the influence of the streamwise vorticity on the evolving flow field. Near the lobe troughs, the bypass flow from the long lobe gully is seen to protrude radially inward further than the flow from the short trough into the otherwise unmixed core flow. At $x/H_{\text{eff}} = 6.3$, a significant increase in the Mach number levels is observed due to the increasing velocity in response to the reduction in cross-sectional area at the nozzle outlet. The flow remains subsonic throughout, but is almost choked at the exit plane. The contour distributions at this location are more uniform than seen at the earlier locations, indicating further mixing between the two streams. However, unmixed regions do still remain at this plane and are reflected by the strip of high Mach number near the nozzle wall (unmixed bypass flow) and the low Mach number zone in the lower region of the computational domain near the centre-line (unmixed core flow).

An analysis of the streamwise vorticity field is now presented to understand the nature of the secondary flow field produced by a scarfed mixer and its impact on the mixing between the two streams. Streamwise vorticity contours are presented

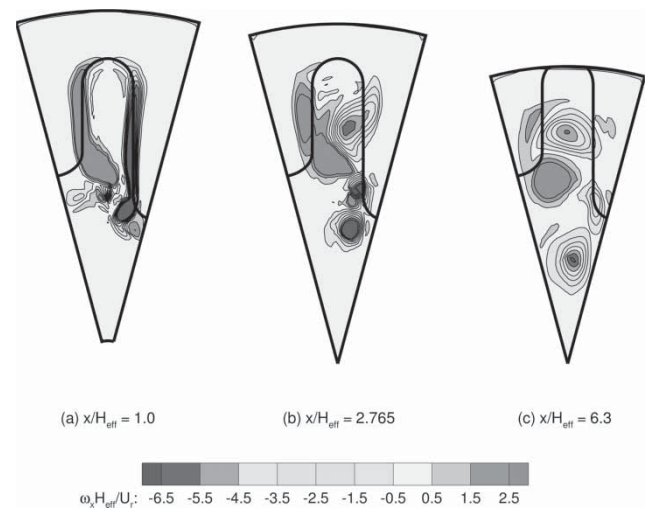


Fig. 15 Non-dimensional streamwise vorticity contours

in Fig. 15 at the same three downstream locations considered earlier. At $x/H_{\text{eff}} = 1.0$, oppositely signed streamwise vorticity is seen to be concentrated along the mixer's vertical side walls. Near the lobe troughs, high concentrations of oppositely signed vorticity exist, which have already begun to depart from the mixer trailing edge geometric profile. This was also observed in the Mach number contours presented earlier. The stronger streamwise vorticity field seen near the lobe troughs relative to values near the lobe peak is related to the mixer surface profile illustrated in Fig. 5. Recalling that the mixer configuration under study consists of a curved surface at the lobe peak, it is clear that the angle of the flow emanating from the trailing edge near the lobe peak is reduced. This is essentially what happens in corrugated splitter plates [28] where the radial velocity components are reduced, leading to a corresponding reduction in the streamwise vorticity. The reduction in the lobe angle at the lobe peak has, therefore, caused the weaker streamwise vorticity field seen in this region. At $x/H_{\text{eff}} = 2.765$, a complex interaction occurs between the adjacent but oppositely signed vorticity fields. The positive vorticity is drawn into the negative vorticity region because of the short/long trough configuration, leading to a breakup of the negative vorticity zone into three separate regions. The interaction is very complex, leading to a highly asymmetric vorticity distribution. At $x/H_{\text{eff}} = 6.3$, the breakup of the negative vorticity zone has led to a vortex being located close to the centre-line. It is this vortex that is responsible for the enhanced mixing of the core flow provided by a scarfed mixer. The scarfing has essentially led to the ejection of vortices towards the engine centre-line, causing extra mixing in that region when compared with a coplanar design. In the upper part of

the flow, the mixing behaviour is dictated by the counter-rotating vortex pair.

The above discussion of the mean flow field evolution now makes it possible to address the important issue of temperature mixing in the scarfed lobed mixer. Contours of the normalized total temperature at the three downstream locations considered so far are given in Fig. 16. The temperature field exhibits a similar distribution to the Mach number contours presented earlier. The interface between the two streams, however, is more clearly defined in the temperature contours at all three locations. Furthermore, the temperature field is, of course, not sensitive to the reduction in cross-sectional area near the exit plane of the mixing duct, as observed in the Mach number contours. The temperature field, therefore, provides a better measure for assessing the level of mixing taking place between the two streams.

At $x/H_{\text{eff}} = 1.0$, the interface between the hot and cold flows is aligned with the mixer's trailing edge except near the lobe troughs, which is clearly reminiscent of the Mach number distributions observed earlier. The interface is more clearly defined with total temperature contours, as no smearing is introduced near the lobe troughs because of boundary layer thickening. At $x/H_{\text{eff}} = 2.765$, the deeper penetration of the long trough bypass flow into the core flow can be seen to be augmented by the presence of the clockwise vortex that distorts the interface between the two streams and increases the interfacial area for mixing. The secondary flow field at slightly longer radial locations is dominated by the counter-rotating vortex pair, which again has led to the breaking up of the hot core flow into two separate regions. This mimics the behaviour seen in the Mach number. Further downstream at

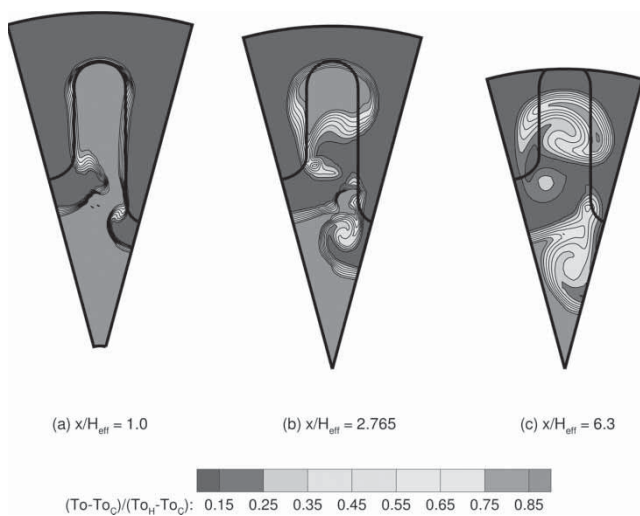


Fig. 16 Non-dimensional total temperature contours

$x/H_{\text{eff}} = 6.3$, the interface continues to stretch as streamwise vorticity continues to have an effect and diffusive mixing across the interface becomes more evident. At this location, the main hot spots that remain are in the hot plume formed in the upper region and the unmixed core flow lying near the centre-line. Unmixed cold regions also remain with the flow just below the nozzle surface being the most significant example of the hot gas in the bypass flow. It is interesting to observe that while the hot plume was located near the lobe peak at $x/H_{\text{eff}} = 2.765$, the hot gas has been shifted lower by $x/H_{\text{eff}} = 6.3$, following the increased velocities associated with the reduction in cross-sectional area.

A clear picture of how the streamwise vorticity contributes to the mixing of the temperature field can be obtained by considering the structure of the flow streamlines within the mixing duct. These streamlines are presented in Fig. 17 with the scalar field representing the total temperature. The three axial planes shown in Fig. 17 correspond to the inlet plane, the plane located at $x/H_{\text{eff}} = 1.0$, and the exit plane at $x/H_{\text{eff}} = 6.3$. The figure illustrates how the streamlines originating in the bypass flow and the core flow interact together to produce the thermal mixing layer. The streamlines in the mixing duct clearly depict two of the three vortices seen in the vorticity contours. These vortices play an important role in mixing the two streams, as indicated by the streamlines associated with these vortices. Also shown is how the upper vortex entrains fluid into its core. For example, consider the streamlines passing through the vertical portion of the mixing layer at the plane $x/H_{\text{eff}} = 1.0$. These streamlines are eventually entrained into the upper vortex further downstream. Regions that are not entrained by the vortices are not fully mixed out as seen from the streamlines that remain unmixed up to the exit plane.

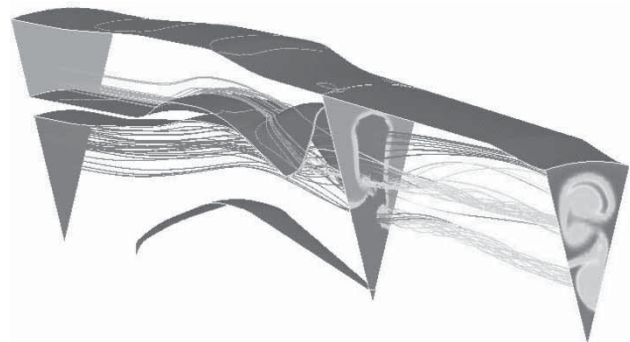


Fig. 17 Streamlines within the mixing duct of the scarfed mixer with contours of total temperature

These results have provided a clear picture of the mixing mechanisms of a scarfed mixer configuration. To assess the extent to which the simulations provide a good representation of the thermal mixing layer, comparisons with the experimental data are necessary. For the scarfed mixer studied here, the only experimental data available were the total temperature field [10]. As the temperature mixing is strongly influenced by the mean flow as discussed earlier, a comparison of the temperature field is believed to reveal the general predictive capability of the current formulation with a $k-\varepsilon$ turbulence model of a realistic scarfed mixer flow field. Measurements of the temperature field were obtained over a 180° sector. To aid in directly comparing measurements and predictions, an identical region containing the predicted temperature field was generated by the repetition of the simulated 30° sector.

Figure 18 shows the 180° annular sector containing the temperature field in both predictions and experiments at $x/H_{\text{eff}} = 2.765$ and $x/H_{\text{eff}} = 6.3$. The experimental measurements shown on the left side of the figure at $x/H_{\text{eff}} = 2.765$ show good circumferential periodicity. The predictions show the same general flow behaviour as seen in the measured data, with the flow in the long lobe troughs penetrating further into the core flow. The measured temperature field shows a higher level of dilution of the thermal mixing layer leading to a more spread out distribution of the contours. In addition, the hot plumes that form near the lobe peaks contain a significantly smaller area of peak temperature than that observed in the predictions, which reveal a larger portion of unmixed core flow. The tightly packed temperature contours in the predictions also indicate a lower level of diffusion than seen in the experiments, a result that is consistent with the velocity comparisons presented by Salman *et al.* [7] for a coplanar lobed mixer. Experiments also reveal that the hot regions are located slightly closer to the outer boundary than that in the predictions. This is likely to be a result of the higher level of diffusion present in the experiments.

At $x/H_{\text{eff}} = 6.3$, the measured temperature field displays a reasonable degree of periodicity in the azimuthal direction. The outer hot spots have almost fully mixed out, although remnants of the hot plumes are clearly visible. The hot core flow located close to the centre-line seen at the upstream location has also undergone a significant level of mixing, leading to a more uniformly distributed temperature field. Corresponding predictions show a similar trend, although the hot regions of the flow have not fully mixed out. In particular, hot regions remain in the plumes and in areas located closer to the centre-line.

The above results indicate that the predicted temperature mixing develops more slowly in the

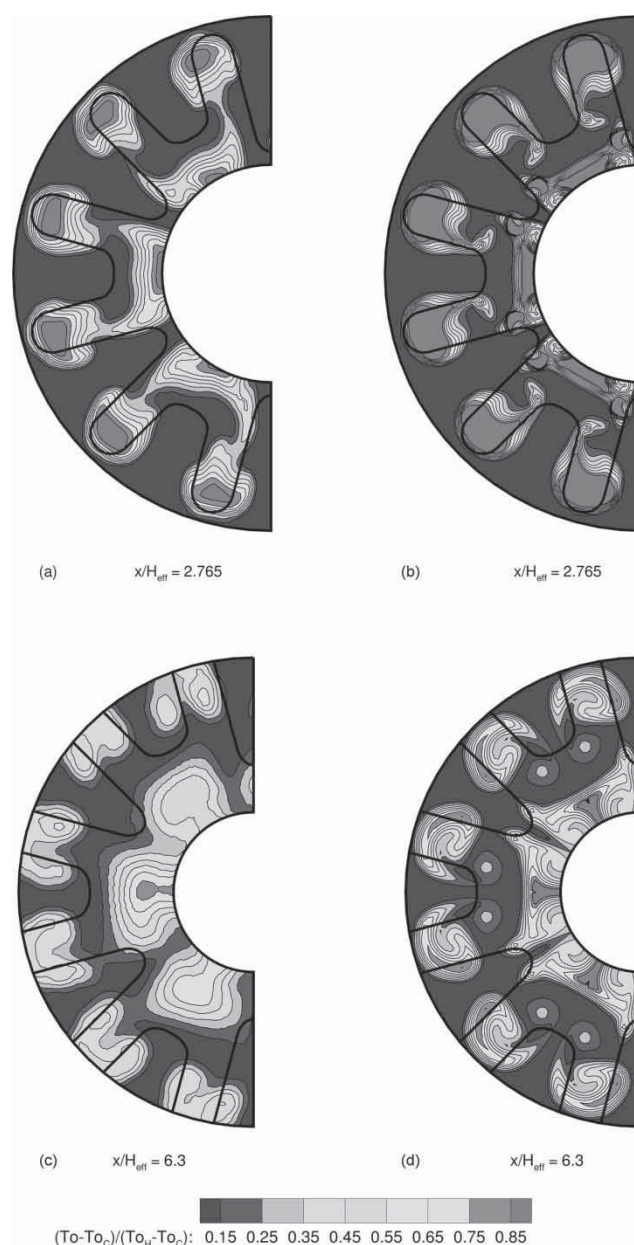


Fig. 18 Comparison of measured and predicted non-dimensionalized total temperature fields (measurements shown on the left-hand side)

predictions than in the experiments. It would be possible to increase the predicted level of turbulent mixing by reducing the value of the turbulent Prandtl number σ_t from 0.9 down to 0.5 or even lower. However, the observed behaviour is analogous to the observations made in the previous isothermal mixer predictions and thus suggests that the key mechanism that is not being correctly predicted by the model is the momentum transport rather than the thermal energy transport. Despite this, the different levels of diffusion observed in the temperature contours imply that the modelling of the turbulent

heat fluxes by a constant turbulence Prandtl number approach is also imperfect.

7 CONCLUSIONS

The high-Reynolds-number $k-\varepsilon$ turbulence model has been implemented into a mixed unstructured grid algorithm as developed by Crumpton *et al.* [14]. A stable time-integration procedure for the turbulence quantities has been developed and the operation of the turbulence model was verified on two elemental flows: the planar mixing layer and the developing boundary layer. Results for these two flows showed very good agreement with the published experimental data and theoretical results.

A grid-type dependency study was conducted for the planar shear layer flow. Three different grid types were used: quadrilateral, triangular grid, and mixed. Simulations revealed that triangular grids were not well suited for predicting shear layer flows in the current algorithm. These flows have the characteristic of a predominant flow direction with strong gradients normal to this direction. Quadrilateral grids were found to be well suited: the alignment of finite value faces with the two directions of characteristic flow behaviour (axial convection and transverse diffusion) gave acceptable levels of numerical smoothing and thus the correct prediction of the turbulent shear layer growth for a given number of node points. A triangular grid with a similar number of nodes gave spurious excess mixing in the initial mixing region because of the numerical smoothing, followed by a reduction in the mixing rate further downstream due to the under-prediction of the turbulence kinetic energy. A corresponding study was performed for the three-dimensional convoluted shear layer of a coplanar lobed mixer geometry using similar three-dimensional grids. These included a purely hexahedral grid, a tetrahedral grid, and a mixed grid. The results for the three-dimensional convoluted mixing layer confirmed the results observed in the planar shear layer case. The tetrahedral grid produced poor predictions of the convoluted shear layer because of excessive numerical smoothing. A mixed grid, with aligned high aspect ratio hexahedral elements in the shear layer region and pyramids and tetrahedra linking to the outer domain, appears to be the optimal grid for this type of problem. However, grid alignment for the convoluted shear layer would require the use of an adaptive method to fully realize the potential of this approach.

Accordingly, a purely hexahedral meshing strategy was adopted for a Reynolds-averaged simulation of a scarfed lobed mixer. The simulations were performed under the non-isothermal flow conditions typically encountered in the engine operation.

Consideration of the predicted Mach number, vorticity, and temperature fields illustrated the complex nature of scarfed mixer flow fields. In particular, strong interactions in the azimuthal direction between the vortices produced by the short and long gullies of the scarfed mixer were observed. This resulted in a change of topology in the streamwise vorticity field, leading to the formation of three vortices within the mixing duct. One vortex was located close to the centre-line and was seen to play an important role in producing enhanced mixing of the core flow. Detailed comparison of the predicted temperature field with measurements reproduced the trends seen in studies of isothermal mixing layer predictions. In particular, although correct trends were observed in comparison with the measured data, the shear layer development occurred more slowly than observed in measurements. The results imply that improvements in predicting lobed mixer flows depend strongly on correctly capturing the momentum transport within the mixing duct.

ACKNOWLEDGEMENTS

The authors would like to acknowledge the funding support for the research work reported here from the Engineering and Physical Sciences Research Council (UK), Grant no. GR/L17863. Financial assistance and technical review monitoring were also provided by Rolls-Royce and DERA; the authors would like to thank, in particular, Dr Paul Strange and Dr Leigh Lapworth (Rolls-Royce) and Mr Craig Mead (DERA). The authors are also grateful for enlightening discussions with Prof. Mike Giles and Dr Pierre Moinier (Oxford University), who provided the unstructured algorithm (HYDRA) used in this work.

REFERENCES

- 1 **Abolfadl, M. A.** and **Sehra, A. K.** *Application of three-dimensional viscous analysis to turbofan forced mixers.* AIAA paper 91-0131, 1991.
- 2 **Malecki, R. E.** and **Lord, W. K.** *Navier-Stokes analysis of a lobed mixer and nozzle.* AIAA paper 90-0453, 1990.
- 3 **O'Sullivan, M. N., Krasnodebski, J. K., Waitz, I. A., Greitzer, E. M., Tan, C. S., and Dawes, W. N.** Computational study of viscous effects on lobed mixer flow features and performance. *J. Propul. Power*, 1996, **12**(3), 449–456.
- 4 **Salman, H.** *Numerical simulation of streamwise vorticity enhanced mixing.* PhD Thesis, Loughborough University, UK, 2001.
- 5 **Koutmos, P.** and **McGuirk, J. J.** Turbofan forced mixer/nozzle temperature and flow field modelling. *Int. J. Heat Mass Transf.*, 1989, **32**(6), 1141–1153.

- 6 **Salman, H., McGuirk, J. J., and Page, G. J.** *A numerical study of vortex interactions in lobed mixer flow fields.* AIAA paper 99-3409, 1999.
- 7 **Salman, H., Page, G. J., and McGuirk, J. J.** Prediction of lobed mixer vortical structures with a $k-\varepsilon$ turbulence model. *AIAA J.*, 2003, **41**(5), 878–887.
- 8 **Yu, S. C. M. and Yip, T. H.** Measurements of velocities in the near field of a lobed forced mixer trailing edge. *Aeronaut. J.*, 1997, **101**(1003), 121–129.
- 9 **McCormick, D. C. and Bennett, J.C., Jr.** Vortical and turbulent structure of a lobed mixer free shear layer. *AIAA J.*, 1994, **32**(9), 1852–1859.
- 10 **Mead, C. J.** *Jet pipe temperature traverses at axial stations downstream of several model-scale forced mixers.* DRA (Pyestock) Noise, vol. 132/97, July 1997.
- 11 **Rollin, G., Duparcq, J. L., and Joubert, H.** Application of a 3D Navier–Stokes solver to analyse the performance of a lobed mixer. ICAS Proceedings, Anaheim, USA, vol. 13, September, 1994, pp. 2128–2135.
- 12 **Launder, B. E. and Spalding, D. B.** The numerical computation of turbulent flows. *Comp. Methods Appl. Mech. Eng.*, 1974, **3**, 269–289.
- 13 **Liu, F. and Zheng, X.** A strongly coupled time-marching method for solving the Navier–Stokes and $k-\omega$ turbulence model equations with multigrid. *J. Comput. Phys.*, 1996, **128**, 289–300.
- 14 **Crumpton, P. I., Moinier, P., and Giles, M. G.** An unstructured algorithm for high Reynolds number flows on highly stretched grids. Proceedings of the 10th International Conference on *Numerical Methods in laminar and turbulent flow*, Pineridge Press, Swansea, UK, 1997, pp. 561–572.
- 15 **Moinier, P.** *Algorithm developments for an unstructured viscous flow solver.* PhD Thesis, University of Oxford, UK, Trinity Term, 1999.
- 16 **Gerolymos, G. A.** Implicit multiple-grid solution of the compressible Navier–Stokes equations using $k-\varepsilon$ turbulence closure. *AIAA J.*, 1990, **28**(10), 1707–1717.
- 17 **Kunz, R. F. and Lakshminarayana, B.** Explicit Navier–Stokes computation of cascade flows using the $k-\varepsilon$ turbulence model. *AIAA J.*, 1992, **30**(1), 13–22.
- 18 **Kunz, R. F. and Lakshminarayana, B.** Stability of explicit Navier–Stokes procedures using $k-\varepsilon$ and $k-\varepsilon/l$ algebraic Reynolds stress turbulence models. *J. Comput. Phys.*, 1992, **103**, 141–159.
- 19 **Mavriplis, D. J. and Martinelli, L.** Multigrid solution of compressible turbulent flow on unstructured meshes using a two-equation model. *Int. J. Numer. Methods Fluids*, 1994, **18**, 887–914.
- 20 **Spalart, P. R. and Allamaras, S. R.** *A one-equation turbulence model for aerodynamic flows.* AIAA paper 92-439, Reno, NV, 1992.
- 21 **Bardina, J. E., Huang, P. G., and Coakley, T. J.** *Turbulence modeling validation, testing, and development.* TM-110446, NASA, 1997.
- 22 **Coles, D.** The law of the wake in the turbulent boundary layer. *J. Fluid Mech.*, 1956, **1**, 191–226.
- 23 **Liepmann, H. W. and Laufer, J.** *Investigations of free turbulent mixing.* TN-1257, NACA, 1947.
- 24 **Launder, B. E. and Sharma, B. I.** Application of the energy dissipation model of turbulence to the calculation of flow near a spinning disc. *Lett. Heat Mass Transf.*, 1974, **1**(2), 131–138.
- 25 **Holmes, P., Lumley, J. L., and Berkooz, G.** *Turbulence, coherent structures, dynamical systems and symmetry.* Cambridge monographs on mechanics, 1998, (Cambridge University Press).
- 26 **Townsend, A. A.** *The structure of turbulent shear flow*, 2nd edition, 1976 (Cambridge University Press).
- 27 **Wilcox, D. C.** *Turbulence modeling for CFD*, 1994, (DCW Industries, Inc.).
- 28 **Belovich, V. M., Samimy, M., and Reeder, M. F.** Dual stream axisymmetric mixing in the presence of axial vorticity. *J. Propul. Power*, 1996, **12**(1), 178–185.